The Astrophysical Journal, 922:114 (19pp), 2021 December 1 https://doi.org/10.3847/1538-4357/ac2578

Extensive Lensing Survey of Optical and Near-infrared Dark Objects (El Sonido): HST *H*-faint Galaxies behind 101 Lensing Clusters

Fengwu Sun[1], Eiichi Egami[1], Pablo G. Pérez-González[2], Ian Smail[3], Karina I. Caputi[4,5], Franz E. Bauer[6,7], Timothy D. Rawle[8], Seiji Fujimoto[5,9], Kotaro Kohno[10,11], Ugnė Dudzevičiūtė[3], Hakim Atek[12], Matteo Bianconi[13], Scott C. Chapman[14], Francoise Combes[15,16], Mathilde Jauzac[17,18,19,20], Jean-Baptiste Jolly[21], Anton M. Koekemoer[22], Georgios E. Magdis[5,9,23], Giulia Rodighiero[24,25], Wiphu Rujopakarn[26,27,28], Daniel Schaerer[29], Charles L. Steinhardt[5,9], Paul Van der Werf[30], Gregory L. Walth[31], and John R. Weaver[5,9]

[1] Steward Observatory, University of Arizona, 933 N. Cherry Avenue, Tucson, AZ 85721, USA; fengwusun@email.arizona.edu
[2] Centro de Astrobiología, Departamento de Astrofísica, CSIC-INTA, Cra. de Ajalvir km.4 E-28850–Torrejón de Ardoz, Madrid, Spain
[3] Centre for Extragalactic Astronomy, Department of Physics, Durham University, South Road, Durham, DH1 3LE, UK
[4] Kapteyn Astronomical Institute, University of Groningen, P.O. Box 800, 9700AV Groningen, The Netherlands
[5] Cosmic Dawn Center (DAWN), Jagtvej 128, DK-2200 Copenhagen N, Denmark
[6] Instituto de Astrofsica, Facultad de Fsica, Pontificia Universidad Catolica de Chile Av. Vicuna Mackenna 4860, 782-0436 Macul, Santiago, Chile
[7] Millennium Institute of Astrophysics (MAS), Nuncio Monse nor Santero Sanz 100, Providencia, Santiago, Chile
[8] European Space Agency (ESA), ESA Office, Space Telescope Science Institute, 3700 San Martin Drive, Baltimore, MD 21218, USA
[9] Niels Bohr Institute, University of Copenhagen, Lyngbyvej 2, DK-2100 Copenhagen Ø, Denmark
[10] Institute of Astronomy, Graduate School of Science, The University of Tokyo, 2-21-1 Osawa, Mitaka, Tokyo 181-0015, Japan
[11] Research Center for the Early Universe, School of Science, The University of Tokyo, 7-3-1 Hongo, Bunkyo-ku, Tokyo 113-0033, Japan
[12] Institut d'Astrophysique de Paris, Sorbonne Universite, CNRS, UMR 7095, 98 bis bd Arago, F-75014 Paris, France
[13] School of Physics & Astronomy, University of Birmingham, Birmingham, B15 2TT, UK
[14] Eureka Scientific, Inc. 2452 Delmer Street Suite 100, Oakland, CA 94602-3017, USA
[15] Sorbonne Université, Observatoire de Paris, Université PSL, CNRS, LERMA, F-75014 Paris, France
[16] Collège de France, 11 Place Marcelin Berthelot, 75231 Paris, France
[17] Centre for Extragalactic Astronomy, Durham University, South Road, Durham DH1 3LE, UK
[18] Institute for Computational Cosmology, Durham University, South Road, Durham DH1 3LE, UK
[19] Astrophysics Research Centre, University of KwaZulu-Natal, Westville Campus, Durban 4041, South Africa
[20] School of Mathematics, Statistics & Computer Science, University of KwaZulu-Natal, Westville Campus, Durban 4041, South Africa
[21] Department of Space, Earth and Environment, Chalmers University of Technology, Onsala Space Observatory, SE-439 92 Onsala, Sweden
[22] Space Telescope Science Institute, 3700 San Martin Drive, Baltimore, MD, 21218, USA
[23] DTU-Space, Technical University of Denmark, Elektrovej 327, DK-2800 Kgs. Lyngby, Denmark
[24] Dipartimento di Fisica e Astronomia, Università di Padova, vicolo dell'Osservatorio 3, I-35122 Padova, Italy
[25] INAF—Osservatorio Astrofisico di Padova, vicolo dell'Osservatorio 5, I-35122 Padova, Italy
[26] Department of Physics, Faculty of Science, Chulalongkorn University, 254 Phayathai Road, Pathumwan, Bangkok 10330, Thailand
[27] National Astronomical Research Institute of Thailand (Public Organization), Don Kaeo, Mae Rim, Chiang Mai 50180, Thailand
[28] Kavli Institute for the Physics and Mathematics of the Universe (WPI),The University of Tokyo Institutes for Advanced Study, The University of Tokyo, Kashiwa, Chiba 277-8583, Japan
[29] Observatoire de Genève, Université de Genève, 51, Ch. des Maillettes, 1290 Versoix, Switzerland
[30] Leiden Observatory, Leiden University, P.O. Box 9513, NL-2300 RA Leiden, The Netherlands
[31] The Observatories of the Carnegie Institution for Science, 813 Santa Barbara Street, Pasadena, CA 91101, USA
Received 2021 May 15; revised 2021 September 7; accepted 2021 September 8; published 2021 November 25

Abstract

We present a Spitzer/IRAC survey of *H*-faint ($H_{160} \gtrsim 26.4$, $< 5\sigma$) sources in 101 lensing cluster fields. Across a CANDELS/Wide-like survey area of $\sim$648 arcmin^2 (effectively $\sim$221 arcmin^2 in the source plane), we have securely discovered 53 sources in the IRAC Channel-2 band (CH2, 4.5 μm; median CH2 $= 22.46 \pm 0.11$ AB mag) that lack robust HST/WFC3-IR F160W counterparts. The most remarkable source in our sample, namely ES-009 in the field of Abell 2813, is the brightest *H*-faint galaxy at 4.5 μm known so far (CH2 $= 20.48 \pm 0.03$ AB mag). We show that the *H*-faint sources in our sample are massive (median $M_{\rm star} = 10^{10.3\pm0.3}\ M_\odot$), star-forming (median star formation rate $=100^{+60}_{-40}\ M_\odot\ {\rm yr}^{-1}$), and dust-obscured ($A_V = 2.6 \pm 0.3$) galaxies around a median photometric redshift of $z = 3.9 \pm 0.4$. The stellar continua of 14 *H*-faint galaxies can be resolved in the CH2 band, suggesting a median circularized effective radius ($R_{\rm e,circ}$; lensing corrected) of 1.9 ± 0.2 kpc and <1.5 kpc for the resolved and whole samples, respectively. This is consistent with the sizes of massive unobscured galaxies at $z \sim 4$, indicating that *H*-faint galaxies represent the dusty tail of the distribution of a wider galaxy population. Comparing with the ALMA dust continuum sizes of similar galaxies reported previously, we conclude that the heavy dust obscuration in *H*-faint galaxies is related to the compactness of both stellar and dust continua ($R_{\rm e,circ} \sim 1$ kpc). These *H*-faint galaxies make up 16^{+13}_{-7}% of the galaxies in the stellar-mass range of $10^{10} - 10^{11.2}\ M_\odot$ at $z = 3 \sim 5$, contributing to 8^{+8}_{-4}% of the cosmic star formation rate density in this epoch and likely tracing the early phase of massive galaxy formation.

Unified Astronomy Thesaurus concepts: Galaxy evolution (594); Infrared galaxies (790); High-redshift galaxies (734); Starburst galaxies (1570); Gravitational lensing (670)

1. Introduction

Dust obscuration is known to play a critical role in reshaping the appearance of star-forming galaxies from the local Universe to the epoch of reionization (e.g., Riechers et al. 2013; Strandet et al. 2017; Marrone et al. 2018; Tamura et al. 2019; Bakx et al. 2020). Significant dust absorption of the rest-frame UV-optical light is an indispensable physical process to produce the thermal continuum radiation seen in the far-infrared (far-IR). This is typically observed at flux densities of $\gtrsim$1 mJy shortward of 1 mm in the submillimeter galaxies (SMGs) that are discovered in abundance at $z \simeq 1$–4 (see reviews in Casey et al. 2014a; Hodge & da Cunha 2020). The high observed dust-to-stellar luminosity ratio and red stellar continuum color of SMGs suggest a high dust attenuation, which is typically $A_V \gtrsim 2$ (e.g., da Cunha et al. 2015; Dudzevičiūtė et al. 2020, 2021).

Among all the SMGs discovered routinely since the end of the last century, the optically faint SMG population has been of particular interest (e.g., Dey et al. 1999; Smail et al. 1999; Bertoldi et al. 2000; Frayer et al. 2000, 2004; Dannerbauer et al. 2002; Wang et al. 2007; Tamura et al. 2010). Identified at millimeter wavelengths with large IR luminosities ($L_{\rm IR} \gtrsim 10^{12}$ $L_\odot$), these galaxies are found to be faint or even undetected in the optical/near-IR, suggesting heavily reddened stellar continua due to strong dust obscuration and/or high redshift ($z \gtrsim 3$). This was highlighted by the study of HDF850.1, the brightest 850 μm source discovered in the Hubble Deep Field (Hughes et al. 1998), which was confirmed later to be an optical/near-IR-faint galaxy ($I \gtrsim 29$, $K \sim 23.5$, Dunlop et al. 2004; Cowie et al. 2009) at $z = 5.18$ with millimeter interferometry (Walter et al. 2012). Later ALMA continuum observations suggested that 15%∼20% of SMGs remain undetected in deep ground-based near-IR images ($K > 24.4$, Simpson et al. 2014; $K > 25.3$, Dudzevičiūtė et al. 2020; Smail et al. 2021). Similar percentages of optical/near-IR-dark SMGs were also presented by studies based on deep HST/WFC3-IR F160W data ($H_{160} > 27$, Chen et al. 2015; Franco et al. 2018), and these galaxies are often referred to as HST-dark, *H*-dropout, or *H*-faint galaxies (e.g., Yamaguchi et al. 2019; Wang et al. 2019).

These optical/near-IR-faint SMGs are likely highly dust-obscured analogs of local ultraluminous infrared galaxies (ULIRGs, $L_{\rm IR} \simeq 10^{12} - 10^{13}$ $L_\odot$), which can be undetectable at high redshift even with deep optical/near-IR imaging (e.g., Dey et al. 1999; Chapman et al. 2001, 2002; Frayer et al. 2004; Smail et al. 2021). This implies that the current mass-selected galaxy sample at $z \gtrsim 4$ (de facto based on observed H/K-band photometric catalogs) may miss a substantial fraction of dusty galaxies at the most massive end ($M_{\rm star} \gtrsim 10^{11}$ $M_\odot$; e.g., Caputi et al. 2015; Wang et al. 2016; Alcalde Pampliega et al. 2019). These sources can contribute to ∼10% of the cosmic star formation rate density (CSFRD) at $z \simeq 3$–5 (Wang et al. 2019; Williams et al. 2019; Yamaguchi et al. 2019; Bouwens et al. 2020; Dudzevičiūtė et al. 2020), and thus the latest ALMA-based CSFRD can be higher than the previous UV/optical estimates in this redshift range (Gruppioni et al. 2020). Furthermore, the red stellar continuum colors of these optical/near-IR-faint SMGs make them natural contaminants of quiescent/post-starburst galaxy samples at $z \simeq 3$–4 (e.g., Simpson et al. 2017a; Schreiber et al. 2018b).

An efficient selection of optical/near-IR-faint SMGs can also be initiated from IR imaging surveys with deep *H*/*K*-band and Spitzer/IRAC (Fazio et al. 2004) coverage (e.g., Ivison et al. 2004; Rodighiero et al. 2007; Huang et al. 2011; Wang et al. 2012; Caputi et al. 2012, 2014; Wang et al. 2016; Alcalde Pampliega et al. 2019). These IRAC-selected extremely red objects (EROs) are the higher-redshift extension of optical/near-IR-selected objects (e.g., Smail et al. 2002; McCarthy 2004), which consist of both dusty star-forming and evolved passive systems. As highlighted in Wang et al. (2019), 39 out of the 63 *H*-faint galaxies ($H_{160} \gtrsim 27$ and CH2 < 24) in the CANDELS fields (Grogin et al. 2011; Koekemoer et al. 2011) were found to be brighter than 0.6 mJy at 870 μm, suggesting a typical SFR of $\sim 310\, M_\odot\ {\rm yr}^{-1}$. These ALMA-detected *H*-faint galaxies, found in abundance ($\sim 530\ {\rm deg}^{-2}$ by Wang et al. 2019), are proposed as a critical tracer of the early phase of massive galaxy formation history. However, most of their physical properties still remain highly uncertain except for rare cases with spectroscopic confirmations (e.g., Walter et al. 2012; Wang et al. 2019; Umehata et al. 2020; Zhou et al. 2020; Caputi et al. 2021; Mitsuhashi et al. 2021) due to their non-detections and faintness at most wavelengths.

In this work, we conduct an Extensive Lensing Survey of Optical/Near-IR Dark Objects (El Sonido). This is a Spitzer/IRAC survey of *H*-faint galaxies in 101 lensing cluster fields with archival HST/WFC3-IR F160W data at a median 5σ depth of $H_{160} \sim 26.4$. Across a CANDELS/Wide-like total survey area of $\sim 648\ {\rm arcmin}^2$ (effectively $\sim 221\ {\rm arcmin}^2$ in the source plane), the depth of this data set is also CANDELS-like ($H_{160} > 27$) assuming a typical lensing magnification of $\mu = 2$. We identify 53 *H*-faint galaxies that are robustly detected at S/N > 5 in the IRAC/CH2 band (median CH2 = 22.46 ± 0.11) but without a significant counterpart in the F160W band (S/N < 5). This yields a Wang et al. (2019)-like sample but about two times brighter owing to the lensing magnification, facilitating further imaging and spectroscopic observations with ALMA and JWST. Moreover, lensing magnification also allows us to spatially resolve the less obscured stellar continua of 14 strongly magnified *H*-faint galaxies with Spitzer/IRAC at 4.5 μm. A comparable study for the unlensed sample will not be possible until the operation of JWST.

This paper is arranged as follows: Section 2 introduces the massive galaxy cluster sample and all the utilized HST, Spitzer, and Herschel data as well as the corresponding data-reduction procedures. Section 3 describes the fundamental measurements with our data, including the source selection, photometry, surface brightness profile modeling, and stacking analysis. In Section 4, we present and discuss the physical properties of *H*-faint galaxies. The conclusions can be found in Section 5. Throughout this paper, we assume a flat ΛCDM cosmology ($h = 0.7$, $\Omega_m = 0.3$) and a Chabrier (2003) initial mass function. The AB magnitude system (Oke & Gunn 1983) is used to express source brightnesses in the near/mid-IR.

2. Data

2.1. The Cluster Sample

We have selected 101 lensing cluster fields with sufficient imaging data to search for *H*-faint galaxies. This sample includes clusters from four subsets: (i) six HST Frontier Field clusters (HFF, Lotz et al. 2017; same as BUFFALO, Steinhardt et al. 2020), (ii) 21 CLASH clusters (Postman et al. 2012), (iii) 41 RELICS clusters (Coe et al. 2019), and (iv) 33 additional clusters observed by the two Herschel Key Programs, the Herschel Lensing Survey (HLS;

Egami et al. 2010; Sun et al. 2021) and the Local Cluster Substructure Survey (LoCuSS; Smith et al. 2010) with archival HST/WFC3-IR F160W imaging data on MAST[32] that were publicly available as of November 2020. All of these clusters have been observed by HST/WFC3-IR in the F160W band and Spitzer/IRAC in the CH1/CH2 at various depths, as further discussed in Appendix A.

2.2. WFC3-IR and IRAC Data

We briefly summarize the utilized HST/WFC3-IR F160W, Spitzer/IRAC CH1 (3.6 μm), and CH2 (4.5 μm) data of the 101 lensing cluster fields in Table 1, including the observation program IDs, total archival scientific integration time ($t_{\rm obs}$), and 5σ depths.

WFC3-IR F160W data are taken from 67 HST observation programs. We obtained a uniform reduction of the data with a standard DRIZZLEPAC v3.1.8 (Gonzaga et al. 2012) routine. Our data processing started from the calibrated, flat-fielded, individual exposures ("_FLT" images). If multiple observation sessions were found, we would compute and correct the internal astrometric offset between individual exposures based on the archival drizzled products ("_DRZ" images). We adopted a PIXFRAC parameter of 0.8 and an output pixel size of $0\farcs06\,{\rm pixel}^{-1}$. For the simplicity of data processing in the six HFF clusters, we only used the data taken by the BUFFALO program (GO 15117, PI: Steinhardt; Steinhardt et al. 2020) because of (i) a larger sky coverage than the original HFF data (Lotz et al. 2017) and (ii) a nearly consistent depth of F160W data as those of the other 95 fields. If an *H*-faint source lies in the area that HFF covered, we use the image products[33] processed by the HFF team.

IRAC CH1 and CH2 data were taken from 68 Spitzer observing programs. For simplicity, we directly used the reduced Spitzer Frontier Field data (Lotz et al. 2017) for the six HFF clusters. In the remaining 95 cluster fields where the IRAC data are generally much shallower than those of the HFF, we reduced the data uniformly using a standard MOPEX routine. Our IRAC data processing started from the archival level 1 (BCD) products, and the output pixel size was set as $0\farcs6\,{\rm pixel}^{-1}$.

The output frames of our WFC3-IR and IRAC image products were registered with the Gaia DR2 (Gaia Collaboration et al. 2018). We first extracted source catalogs in the IRAC bands with SEXTRACTOR (Bertin & Arnouts 1996) and cross-matched with the Gaia catalog (typically 20–30 stars) to correct the world coordinate system (WCS) offsets. This achieved a final astrometric error of $\lesssim 0\farcs1$ in IRAC CH1/2. Because the field of view (FoV) of WFC3-IR is only 4.6 arcmin^2, much smaller than the area of IRAC image products, it is very likely that the number of Gaia stars falling in the WFC3-IR coverage is not large enough for a reliable astrometric registration. Therefore, we registered the output frames of WFC3-IR images using the astrometry-corrected IRAC CH1 images with a similar source extraction and cross-matching pipeline. The absolute astrometric error in WFC3-IR images was comparable to that of the IRAC images as a consequence.

[32] Mikulski Archive for Space Telescopes (MAST), https://archive.stsci.edu/.
[33] https://archive.stsci.edu/prepds/frontier/

2.3. Ancillary Data

In order to further characterize the *H*-faint sample, we include other ancillary data for the 32 cluster fields in which we have identified *H*-faint sources (see Section 3). The final constructed data set in these fields therefore consists of data in 15 bands, namely (1) five HST bands: WFC3-IR F105W, F110W, F125W, F140W, and F160W, (2) five Spitzer bands: IRAC CH1, CH2, CH3 (5.8 μm), CH4 (8.0 μm), and MIPS 24 μm (Rieke et al. 2004), and (3) five Herschel bands: PACS 100, 160 μm (Poglitsch et al. 2010), SPIRE 250, 350, and 500 μm (Griffin et al. 2010).

2.3.1 HST Data

Based on an archival search, we have found WFC3-IR/F105W data in 30 out of the 32 clusters, F110W in 8, F125W in 28, and F140W in 22. The data-reduction routine is the same as described in Section 2.2. Note that we only processed the BUFFALO data (F105W and F125W) for the HFF clusters. For sources that are within the coverage of the original HFF data, we directly used the F105W, F125W, and F140W data reduced by the HFF team. The expected depth of HST/ACS F814W data is comparable to that observed in the WFC3-IR F105W band. Because of the non-detection of the stacked sources in F105W band (Section 3.4) and the heavily reddened stellar continuum, we do not expect F814W and bluer HST data to provide any useful spectral energy distribution (SED) constraint. Therefore, we did not include any HST/ACS data for the analysis.

2.3.2 Spitzer Data

We identified archival IRAC CH3 and CH4 data for 10 out of the 32 cluster fields with *H*-faint objects, and the data were processed using the same method as described in Section 2.2. We also included MIPS 24 μm data for 13 cluster fields. MIPS data reduction started from the archival post-BCD products, and we used MOPEX v1.8 for the flat-fielding, artifact removal, and image mosaicking. The output pixel size is $1\farcs2\,{\rm pixel}^{-1}$, and the typical beam size is 6″.

2.3.3 Herschel Data

Herschel/PACS data at 100 and 160 μm are available for 17 cluster fields; 16 of these clusters were observed by the HLS (Egami et al. 2010) and A370 was observed by the PACS Evolutionary Probe (PEP; Lutz et al. 2011). The observational settings and reduction of PACS data were detailed in Rawle et al. (2016) and Sun et al. (2021) and the output pixel scale is $1''\,{\rm pixel}^{-1}$ at 100 μm and $2''\,{\rm pixel}^{-1}$ at 160 μm. The typical resolution of PACS data is 7″ at 100 μm and 12″ at 160 μm. Herschel/SPIRE data at 250, 350, and 500 μm are available for all the 32 cluster fields. Among them, 16 cluster fields were observed by the HLS in the "deep" mode to the confusion-limit depth (rms $\sim$ 6 mJy/beam at 250 μm), and 14 cluster fields were observed by the HLS in the "snapshot" mode (rms$\sim$10 mJy/beam at 250 μm). The remaining two clusters, A370 and CLJ0152.7-1357, were observed as parts of the Herschel Multi-tiered Extragalactic Survey (HerMES; Oliver et al. 2012) to the confusion-limit depth. The observational settings of the HLS clusters and the data-reduction procedure were described in Rawle et al. (2016) and Sun et al. (2021). The output pixel sizes are 6″, 9″, and 12″ at 250–500 μm, which are about one-third of the beam sizes in the corresponding bands.

Table 1
El Sonido Cluster Sample

#	Cluster Name	Coordinates		HST/WFC3-IR F160W				Spitzer/IRAC CH1&2	
		R.A. (deg)	Decl. (deg)	TP[a]	t_{obs}[b] (h)	Depth[c] (mag)	Program[d]	Depth[e] (mag)	Program[f]
1	MACS1149	177.388	22.391	HFF/BUFFALO	40.93/1.79	26.5	1, 2, 3, 4, 5, 6, 7, 8, 9	24.4	1, 2, 3
2	A370	39.939	−1.549	HFF/BUFFALO	24.48/1.79	26.1	3, 8, 10, 11, 12	23.9	1, 4, 5, 6
3	A2744	3.583	−30.387	HFF/BUFFALO	22.35/1.79	26.5	8, 13, 14	24.0	7, 8
4	MACS0416	64.018	−24.088	HFF/BUFFALO	22.34/1.79	26.3	8, 13, 15, 16	24.6	9, 10
5	MACS0717	109.427	37.738	HFF/BUFFALO	21.90/1.79	26.4	8, 17, 18	23.8	1, 2, 11, 12
6	AS1063	342.204	−44.536	HFF/BUFFALO	21.81/1.79	26.2	8, 19, 20	24.1	1, 7, 13
7	BULLET	104.630	−55.947	⋯	4.69	26.6	10, 21	23.0	1, 2, 14, 15
8	0205–5829	31.420	−58.488	⋯	3.30	26.8	22, 23, 24	22.9	16, 17
9	A1763	203.800	41.000	RELICS	2.98	26.0	25	23.0	18, 19, 20, 21
10	MACS1423	215.951	24.074	CLASH	2.65	27.1	13, 26	23.2	1, 2, 22
11	RCS2327	351.870	−2.083	⋯	2.57	26.8	27	23.6	1, 2
12	RXJ1347	206.891	−11.805	CLASH	2.40	26.5	10, 13, 28	23.8	1, 2, 7
13	CLJ0152.7–1357	28.167	−13.955	RELICS	2.24	26.9	25	23.6	18, 19, 23, 24, 25, 26, 27, 28
14	0615–5746	93.953	−57.789	RELICS	2.15	26.8	25, 29	22.9	18, 19, 29, 30
15	2106–5844	316.537	−58.735	⋯	2.12	26.4	24, 30	21.6	31
16	MS2137	325.051	−23.639	CLASH	2.03	26.8	31, 32	23.3	1, 7, 16
17	RBS1748	322.414	0.077	CLASH	1.73	26.4	33	22.4	1, 32, 33, 34
18	2040–4451	310.274	−44.837	⋯	1.68	27.1	22, 23	22.6	30, 35
19	A383	42.020	−3.525	CLASH	1.65	26.3	34, 35	23.1	1, 7, 16
20	0546–5345	86.642	−53.772	⋯	1.56	26.8	24	23.1	31, 36
21	MACS1720	260.039	35.583	CLASH	1.47	26.3	35, 36	23.5	34, 37, 38
22	MACS0647	101.929	70.283	CLASH	1.45	26.6	37	23.0	1, 39
23	A521	73.535	−10.209	⋯	1.45	26.7	38	23.0	1
24	MACSJ0940.9 + 0744	145.202	7.728	⋯	1.45	26.6	39	22.7	40
25	CLJ1226	186.734	33.550	CLASH	1.43	26.9	40	23.1	16, 23, 26, 41
26	A2261	260.586	32.108	CLASH	1.40	26.5	41	23.0	7, 32, 37
27	MACS0329	52.402	−2.222	CLASH	1.40	26.6	42	22.8	9
28	MACSJ1157.3 + 3336	179.296	33.599	CLASH	1.40	26.2	43	23.3	16, 32, 40, 42
29	MACS2129	322.366	−7.696	CLASH	1.40	26.7	44	23.3	1, 2, 43
30	MACS1311	197.782	−3.166	CLASH	1.40	26.8	45	23.5	9, 44
31	A209	22.973	−13.603	CLASH	1.40	26.2	46	23.6	7, 9
32	MACS1206	181.583	−8.785	CLASH	1.40	26.3	47	23.3	9
33	A611	120.233	36.058	CLASH	1.40	26.4	48	23.3	1, 45
34	MACS0744	116.209	39.463	CLASH	1.40	26.8	49	23.4	1, 2
35	RXJ1532	233.258	30.343	CLASH	1.40	26.4	50	23.7	16, 33, 37, 46
36	A1689	197.856	−1.303	⋯	1.40	25.8	51	23.2	7, 16, 32, 47, 48
37	MACS1115	168.943	1.486	CLASH	1.37	26.7	52	23.4	9, 38
38	MACS1931	292.979	−26.552	CLASH	1.34	26.4	53	22.6	9, 49
39	MACS0429	67.380	−2.907	CLASH	1.34	26.8	54	23.2	9
40	A2218	248.968	66.214	⋯	1.34	26.5	10, 55	23.2	7, 47
41	MACSJ2214.9–1359	333.755	−13.971	⋯	1.33	26.7	56	23.6	1, 2
42	MACSJ0723.3–7327	110.883	−73.432	RELICS	1.26	26.7	25	23.0	18, 19, 25, 34
43	A1758	203.173	50.574	RELICS	1.13	26.2	25	23.9	1, 7
44	2344–4243	356.191	−42.693	⋯	1.12	26.7	57	22.7	30, 46, 50
45	MACSJ0159.0–3412	29.765	−34.244	⋯	0.83	26.4	58	22.5	40
46	49187	231.121	9.960	⋯	0.80	27.0	59	23.1	16, 51, 52, 53
47	A1703	198.724	51.812	⋯	0.78	26.4	51	23.5	54
48	RCS0224	36.142	−0.043	⋯	0.73	26.8	60	22.9	1, 55, 56, 57
49	A68	9.288	9.151	⋯	0.67	26.2	10	23.4	1
50	MACSJ0257.6–2209	44.402	−22.172	⋯	0.67	26.4	61	23.0	16, 45
51	AS1077	344.713	−34.801	⋯	0.67	26.5	10	23.3	1, 7, 48
52	A773	139.474	51.731	⋯	0.67	26.0	10	22.9	1, 7, 32, 45
53	A1835	210.267	2.816	⋯	0.67	26.4	10	23.5	1, 4
54	MS0451	73.564	−3.058	⋯	0.67	26.8	10	23.6	1, 2, 7, 43
55	MACSJ2201.9–5956	330.486	−59.977	⋯	0.61	25.8	62	22.9	40
56	MS1358	209.894	62.487	⋯	0.61	26.5	10	23.8	1, 7, 54
57	A665	127.713	65.862	RELICS	0.61	25.8	25	23.0	16, 18, 19
58	MACSJ0035.4–2015	8.850	−20.289	RELICS	0.59	26.4	25	23.3	18, 19
59	PLCKG308.3–20.2	229.608	−81.503	RELICS	0.59	26.0	25	22.9	16, 18, 19, 25, 34, 58
60	PLCKG004.5–19.5	289.271	−33.522	RELICS	0.57	26.2	25	22.5	18, 19, 20
61	PSZ2G138.6–10.8	36.779	49.008	RELICS	0.57	26.7	25	22.2	18, 19, 34
62	RXCJ0142.9 + 4438	25.721	44.639	RELICS	0.57	26.1	25	22.8	18, 19
63	MACSJ0159.8–0849	29.945	−8.858	RELICS	0.56	26.4	25	23.5	16, 18, 19
64	MACSJ0245.5–5302	41.367	−53.065	RELICS	0.56	26.1	25	23.3	18, 19, 36, 59
65	0102–4915	15.703	−49.283	RELICS	0.56	26.9	25	23.4	18, 19, 25, 36
66	MACSJ0417.5–1154	64.370	−11.926	RELICS	0.56	26.0	25	22.8	18, 19, 45
67	MACS0018	4.696	16.415	RELICS	0.56	26.7	25	22.7	7, 18, 19, 60
68	MS1008.1–1224	152.600	−12.644	RELICS	0.56	26.2	25	23.1	18, 19, 25, 48
69	A697	130.732	36.375	RELICS	0.56	26.1	25	23.0	1, 7, 16, 61, 62

Table 1
(Continued)

#	Cluster Name	Coordinates		HST/WFC3-IR F160W				Spitzer/IRAC CH1&2	
		R.A. (deg)	Decl. (deg)	TP[a]	t_{obs}[b] (h)	Depth[c] (mag)	Program[d]	Depth[e] (mag)	Program[f]
70	MACSJ0911.2 + 1746	137.830	17.789	RELICS	0.56	26.7	25	23.4	1, 34, 59
71	RXSJ0603 + 42	90.838	42.232	RELICS	0.56	26.3	25	22.4	18, 19, 25, 32
72	MACSJ1615.7–0608	243.921	−6.165	RELICS	0.56	25.8	25	23.0	18, 19, 32, 48
73	MACSJ0553.4–3342	88.380	−33.684	RELICS	0.55	26.5	25	23.4	18, 19, 45, 59
74	MACSJ1514.9–1523	228.718	−15.413	RELICS	0.55	26.2	25	23.4	16, 18, 19
75	WHLJ0137	24.354	−8.457	RELICS	0.55	26.5	25	23.3	16, 18, 19, 49
76	MACSJ0032.1 + 1808	8.026	18.109	RELICS	0.55	26.4	25	22.8	18, 19, 45
77	PSZ2G209.8 + 10.2	110.596	7.408	RELICS	0.55	26.2	25	22.5	18, 19, 49
78	A2813	10.859	−20.611	RELICS	0.55	26.2	25	23.2	1
79	PLCKG287.0 + 32.9	177.704	−28.085	RELICS	0.55	25.9	25	23.0	18, 19, 20
80	A2537	347.106	−2.206	RELICS	0.55	26.2	25	22.9	1
81	MACSJ0454.1 + 0255	73.559	2.940	RELICS	0.55	26.6	25	23.5	18, 19, 63
82	MACSJ0232.2–4420	38.052	−44.373	RELICS	0.55	26.2	25	23.2	16, 18, 19
83	MACSJ1131.8–1955	173.004	−19.919	RELICS	0.55	26.3	25	23.0	16, 18, 19, 32
84	MACSJ0308.9 + 2645	47.215	26.734	RELICS	0.55	26.3	25	22.8	18, 19
85	MACSJ0257.1–2325	44.267	−23.452	RELICS	0.55	26.7	25	23.3	1
86	MACSJ0600.1–2008	90.067	−20.123	RELICS	0.55	26.4	25	23.0	18, 19, 45
87	MACSJ0358.8–2955	59.688	−29.943	RELICS	0.55	26.4	25	23.3	18, 19
88	MACS0025	6.379	−12.382	RELICS	0.53	26.4	25	23.6	1
89	MACSJ2211.7–0349	332.924	−3.858	RELICS	0.53	26.2	25	23.1	16, 18, 19, 45
90	MACSJ0949.8 + 1708	147.445	17.122	RELICS	0.53	26.0	25	23.0	18, 19
91	MACSJ0312.9 + 0822	48.220	8.352	RELICS	0.53	26.0	25	23.4	16, 18, 19
92	0254–5857	43.518	−58.963	RELICS	0.53	26.5	25	23.2	16, 18, 19
93	MACSJ0138.0–2155	24.498	−21.951	⋯	0.45	26.3	63	22.7	40, 64
94	0151–5954	27.789	−59.905	⋯	0.39	26.6	64	22.8	16, 30
95	34770	182.332	26.688	⋯	0.34	26.4	65	23.3	65, 66
96	34630	174.566	27.936	⋯	0.34	26.5	65	22.6	66, 67
97	MACSJ2243.3–0935	340.831	−9.624	⋯	0.34	26.3	65	22.9	45, 67
98	RXCJ2043.2–2144	310.826	−21.712	⋯	0.34	26.0	61	22.6	45
99	MACSJ0150.3–1005	27.577	−10.122	⋯	0.33	26.3	66	22.9	16, 40, 68
100	MACSJ1717.1 + 2931	259.254	29.498	⋯	0.33	26.3	67	22.4	40
101	26029	215.233	39.935	⋯	0.31	26.3	65	23.0	24, 66, 67

Notes. This table is sorted by the decreasing order of total scientific integration time of archival WFC3-IR/F160W data.
[a] Names of HST Treasury Program.
[b] Total scientific integration time. For each HFF/BUFFALO cluster, the t_{obs} before slash stands for all observations (i.e., both original HFF and BUFFALO), and t_{obs} after slash stands for BUFFALO-only observations (used for source extraction, see Section 2.2) that were split into four separate pointings.
[c] 5σ point-source depth in the F160W band measured with $r = 0\farcs4$ aperture. The depths of HFF clusters are calculated using BUFFALO-only data.
[d] HST observation programs: (1) 12068 (Postman), (2) 13504 (Lotz), (3) 13790 (Rodney), (4) 14041 (Kelly), (5) 14199 (Kelly), (6) 14528 (Kelly), (7) 14872 (Kelly), (8) 15117 (Steinhardt), (9) 15308 (Gonzalez), (10) 11591 (Kneib), (11) 14038 (Lotz), (12) 14216 (Kirshner), (13) 13386 (Rodney), (14) 13495 (Lotz), (15) 12459 (Postman), (16) 13496 (Lotz), (17) 12103 (Postman), (18) 13498 (Lotz), (19) 12458 (Postman), (20) 14037 (Lotz), (21) 11099 (Bradac), (22) 13677 (Perlmutter), (23) 14327 (Perlmutter), (24) 15294 (Wilson), (25) 14096 (Coe), (26) 12790 (Postman), (27) 13177 (Bradac), (28) 12104 (Postman), (29) 15920 (Salmon), (30) 15883 (Schrabback), (31) 12102 (Postman), (32) 12461 (Riess), (33) 12457 (Postman), (34) 12065 (Postman), (35) 12360 (Perlmutter), (36) 12455 (Postman), (37) 12101 (Postman), (38) 15435 (Chisholm), (39) 15696 (Carton), (40) 12791 (Postman), (41) 12066 (Postman), (42) 12452 (Postman), (43) 12787 (Postman), (44) 12100 (Postman), (45) 12789 (Postman), (46) 12451 (Postman), (47) 12069 (Postman), (48) 12460 (Postman), (49) 12067 (Postman), (50) 12454 (Postman), (51) 11802 (Ford), (52) 12453 (Postman), (53) 12456 (Postman), (54) 12788 (Postman), (55) 11143 (Baker), (56) 13666 (Bradac), (57) 15831 (Bayliss), (58) 12197 (Richard), (59) 13767 (Trenti), (60) 14497 (Smit), (61) 14148 (Egami), (62) 12817 (Massey), (63) 14496 (Newman), (64) 14896 (Bayliss), (65) 13003 (Gladders), (66) 14205 (Newman), (67) 15670 (Boehringer).
[e] 5σ depth in the CH2 band measured with $r = 1\farcs8$ aperture.
[f] Spitzer/IRAC observation programs: (1) 60034 (Egami), (2) 90009 (Bradac), (3) 90260 (Soifer), (4) 64 (Fazio), (5) 137 (Fazio), (6) 10171 (Soifer), (7) 83 (Rieke), (8) 90257 (Soifer), (9) 80168 (Bouwens), (10) 90258 (Soifer), (11) 40652 (Kocevski), (12) 90259 (Soifer), (13) 10170 (Soifer), (14) 3550 (Jones), (15) 40593 (Gonzalez), (16) 14253 (Stefanon), (17) 70053 (Brodwin), (18) 12005 (Bradac), (19) 12123 (Soifer), (20) 13165 (Bradac), (21) 20512 (Fadda), (22) 50393 (Kocevski), (23) 17 (Fazio), (24) 10043 (Sheth), (25) 14017 (Bradac), (26) 20740 (Holden), (27) 50726 (Holden), (28) 70063 (Holden), (29) 13210 (Bradac), (30) 80012 (Brodwin), (31) 60099 (Brodwin), (32) 14242 (Stroe), (33) 30659 (O'Dea), (34) 90233 (Lawrence), (35) 12030 (Strazzullo), (36) 70149 (Menanteau), (37) 545 (Egami), (38) 90213 (Bouwens), (39) 10140 (Coe), (40) 12095 (Egami), (41) 40204 (Kennicutt), (42) 11080 (Gonzalez), (43) 50610 (Yun), (44) 10015 (Johnston), (45) 90218 (Egami), (46) 10041 (Colbert), (47) 20439 (Egami), (48) 50096 (Martini), (49) 80162 (Lawrence), (50) 14304 (Stefanon), (51) 11121 (Finkelstein), (52) 40058 (Rines), (53) 80134 (Colbert), (54) 40311 (Lacy), (55) 20754 (Ellingson), (56) 60095 (Gal), (57) 60139 (Richards), (58) 10098 (Stern), (59) 14281 (Bradac), (60) 50138 (Rieke), (61) 3163 (Strauss), (62) 14130 (Bouwens), (63) 3720 (Huang), (64) 12127 (Newman), (65) 13006 (Trilling), (66) 70154 (Gladders), (67) 90232 (Rigby), (68) 12003 (Newman).

3. Source Extraction and Measurements

3.1. Source Extraction and Photometry

To construct a sample of gravitationally lensed *H*-faint galaxies in all 101 cluster fields, we first extracted sources with SExtractor v2.19.5 in both WFC3-IR/F160W and IRAC/CH2 maps. We extracted sources in the CH2 maps instead of the CH1 maps because *H*-faint sources generally show red IRAC colors and thus the CH2 S/N is higher than that in the CH1. We fine-tuned the SExtractor configuration files to request five continuous pixels above 1.8σ for detections in the CH2 band, and 10 continuous pixels above 2σ in the F160W band. We

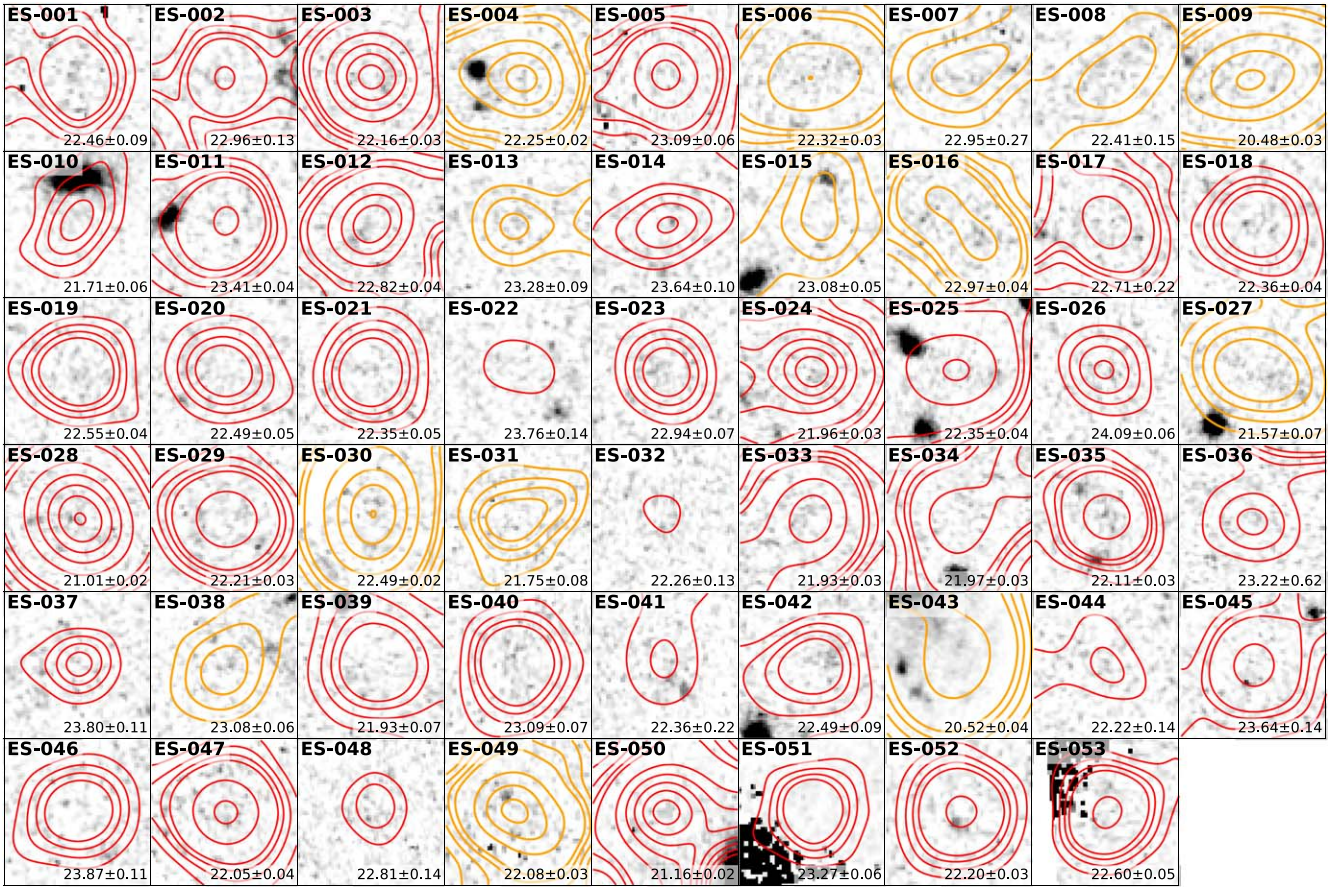

Figure 1. Cutout images of all the 53 *H*-faint sources presented in this work. HST/WFC3-IR F160W images are shown in the background, and Spitzer/IRAC CH2 (4.5 μm) images are shown as red (if unresolved) or orange (if resolved) contours. Contour levels are 4, 6, 8, 10, 20, 30σ ..., from the outside in. The IRAC CH2 magnitude of each source is noted at the lower-right corner of each image. The size of each cutout image is $3\farcs6 \times 3\farcs6$.

also applied an aggressive set of background subtraction (BACK_FILTERSIZE=3, BACK_SIZE=24) and deblending parameters (DEBLEND_MINCONT=10^{-6}) to obtain better source deblending and extraction in crowded fields.

We then cross-matched the extracted F160W and CH2 catalogs to select CH2 sources that (i) are within the F160W coverage and $>1''$ away from the edge and (ii) have no matched F160W counterpart within a maximum separation of $1''$ or the brightness of the matched counterpart (measured by SEXTRACTOR as MAG_AUTO) is fainter than that of the CH2 by at least three magnitudes. We further purified this sample by conducting aperture photometry at the centroids of CH2 sources in the F160W, CH1, and CH2 bands. We adopted fixed aperture sizes of $r = 0\farcs4$ in F160W and $1\farcs8$ in CH1/2, and aperture-correction factors are computed from the corresponding 2D point-spread functions (PSFs; 1.20, 1.42, 1.46 times respectively). We note that the point-source assumption for aperture correction in the F160W band may not be valid because a sample of *H*-faint sources can be resolved even with IRAC (Section 3.2). Assuming exponential source profile with circularized effective radius $R_{\rm e,circ} = R_{\rm e,maj}\sqrt{b/a} = 0\farcs45$ and axis ratio $b/a = 0.2$ for IRAC-resolved sources, and $R_{\rm e,circ} = 0\farcs25$, $b/a = 0.4$ for IRAC-unresolved sources, additional aperture-correction factors of 3.15 and 1.57 times would be needed for both scenarios, respectively. Such types of aperture-correction factors are later applied for the photometry of bright extended sources like ES-009 and stacked sources in Section 3.4. The sky background was subtracted using the median of sigma-clipped local annulus, and a photometric uncertainty was computed using the rms of that. We removed all 110 CH2 sources with F160W counterparts detected above 5σ.

After another round of visual inspection, we further removed 38 spurious sources that were clearly detected in the F160W band but blended in CH2, and four marginally detected CH2 sources without any counterpart in the CH1 band. Therefore, our final *H*-faint source sample consists of 53 sources detected in 32 lensing cluster fields that are (i) undetected in the WFC3-IR/F160W band ($<5\sigma$, typically $H_{160} \gtrsim 26.4$ assuming point-source model), (ii) robustly detected in the IRAC CH2 band at $>5\sigma$ (median CH2 magnitude of CH2 $= 22.46 \pm 0.11$), and (iii) showing a counterpart in the IRAC CH1 band through visual inspection (median CH1 magnitude of CH1 $= 23.00 \pm 0.11$). We assigned IDs for these sources from ES-001 to ES-053 by the increasing order of R.A. (ES=El Sonido). Figure 1 shows the cutout images of all 53 *H*-faint sources in our sample. The coordinates and photometric measurements are presented in Table 2.

We also investigate the source detectability and photometry accuracy in the F160W band with a larger aperture size ($r_{\rm aper} = 0\farcs6$). With this increased aperture, three sources are detected above a 5σ detection threshold (ES-008, ES-041, and ES-042). In two cases (ES-041 and ES-042), the detections are caused by faint clumps offset from the IRAC centroids by $0\farcs5$, which may or may not be associated with the IRAC-detected galaxies. In the case of ES-008, we clearly see a faint extended source, whose significance of detection has increased with a

Table 2
Summary of Measurements in the HST/WFC3-IR F160W and Spitzer/IRAC CH1/CH2 Bands

ID	Coordinates		Cluster Name	HST/WFC3	Spitzer/IRAC			μ[c]
	R.A. (deg)	Decl. (deg)		F160W[a] (mag)	CH1 (mag)	CH2 (mag)	$R_{e,circ}$[b] ($''$)	
ES-001[d]	3.55824	−30.35491	A2744	>26.1	22.77 ± 0.12	22.46 ± 0.09	⋯	2.5
ES-002[d]	3.56268	−30.39096	A2744	>26.4	23.00 ± 0.14	22.96 ± 0.13	⋯	3.2
ES-003[d]	3.57555	−30.42436	A2744	>26.4	22.67 ± 0.05	22.16 ± 0.03	⋯	1.6
ES-004[d]	3.58133	−30.38023	A2744	27.4 ± 0.1	22.71 ± 0.03	22.25 ± 0.02	0.37 ± 0.02	3.3
ES-005[e]	3.62774	−30.39430	A2744	>26.2	23.78 ± 0.12	23.09 ± 0.06	⋯	1.4
ES-006	8.03734	18.14496	MACSJ0032.1 + 1808	>26.6	22.70 ± 0.03	22.32 ± 0.03	0.43 ± 0.17	2.9
ES-007	8.05115	18.14700	MACSJ0032.1 + 1808	>26.5	23.81 ± 0.68	22.95 ± 0.27	0.79 ± 0.08	3.2
ES-008	8.05821	18.14266	MACSJ0032.1 + 1808	>26.6	22.92 ± 0.26	22.41 ± 0.15	0.54 ± 0.07	4.2
ES-009[e]	10.85795	−20.60537	A2813	>26.6	21.29 ± 0.03	20.48 ± 0.03	0.51 ± 0.04	3.3
ES-010	24.52332	−21.92225	MACSJ0138.0–2155	>26.0	21.89 ± 0.06	21.71 ± 0.06	⋯	⋯
ES-011	28.17801	−13.95085	CLJ0152.7–1357	>27.3	23.56 ± 0.04	23.41 ± 0.04	⋯	2.4
ES-012[d]	39.96179	−1.60007	A370	>26.3	23.25 ± 0.05	22.82 ± 0.04	⋯	2.3
ES-013	44.28355	−23.45520	MACSJ0257.1–2325	>26.7	23.55 ± 0.07	23.28 ± 0.09	0.22 ± 0.08	1.0
ES-014	44.30528	−23.42594	MACSJ0257.1–2325	>26.6	25.08 ± 0.75	23.64 ± 0.10	⋯	1.2
ES-015	59.69519	−29.92799	MACSJ0358.8–2955	>26.3	23.29 ± 0.05	23.08 ± 0.05	0.70 ± 0.16	2.3
ES-016	64.04326	−24.11303	MACS0416	>26.5	23.49 ± 0.06	22.97 ± 0.04	0.55 ± 0.12	1.5
ES-017	64.04380	−24.08031	MACS0416	27.2 ± 0.2	23.25 ± 0.33	22.71 ± 0.22	⋯	2.7
ES-018	64.39853	−11.91482	MACSJ0417.5–1154	>26.7	23.05 ± 0.11	22.36 ± 0.04	⋯	1.9
ES-019	64.40427	−11.90550	MACSJ0417.5–1154	>26.7	23.30 ± 0.06	22.55 ± 0.04	⋯	2.7
ES-020	67.38766	−2.86797	MACS0429	>26.5	23.21 ± 0.10	22.49 ± 0.05	⋯	2.1
ES-021	73.51120	2.88566	MACSJ0454.1 + 0255	>26.6	23.19 ± 0.16	22.35 ± 0.05	⋯	⋯
ES-022[d]	73.53382	−10.21773	A521	>27.0	24.98 ± 0.28	23.76 ± 0.14	⋯	⋯
ES-023	88.34406	−33.72470	MACSJ0553.4–3342	>26.8	23.73 ± 0.19	22.94 ± 0.07	⋯	2.6
ES-024[d]	109.40894	37.77138	MACS0717	>26.3	22.45 ± 0.04	21.96 ± 0.03	⋯	2.2
ES-025	110.85850	−73.44440	MACSJ0723.3–7327	>27.0	22.81 ± 0.07	22.35 ± 0.04	⋯	2.2
ES-026	116.21220	39.43703	MACS0744	>26.6	24.46 ± 0.15	24.09 ± 0.06	⋯	1.4
ES-027	116.22664	39.44592	MACS0744	>26.9	22.10 ± 0.11	21.57 ± 0.07	0.29 ± 0.15	2.8
ES-028[e]	130.73140	36.36817	A697	>26.4	21.59 ± 0.03	21.01 ± 0.02	⋯	8.9
ES-029[e]	130.76900	36.36602	A697	>26.0	22.78 ± 0.05	22.21 ± 0.03	⋯	2.6
ES-030	137.82094	17.78358	MACSJ0911.2 + 1746	>26.0	22.77 ± 0.02	22.49 ± 0.02	0.29 ± 0.09	1.2
ES-031	145.22536	7.72584	MACSJ0940.9 + 0744	>26.8	>23.3	21.75 ± 0.08	0.38 ± 0.23	⋯
ES-032	145.23096	7.75463	MACSJ0940.9 + 0744	>26.8	22.99 ± 0.26	22.26 ± 0.13	⋯	⋯
ES-033	172.98836	−19.91272	MACSJ1131.8–1955	>26.6	22.62 ± 0.04	21.93 ± 0.03	⋯	⋯
ES-034	172.98894	−19.91319	MACSJ1131.8–1955	>26.6	22.62 ± 0.03	21.97 ± 0.03	⋯	⋯
ES-035	177.34485	22.40202	MACS1149	>26.1	22.49 ± 0.04	22.11 ± 0.03	⋯	1.3
ES-036	177.36494	22.39943	MACS1149	>26.4	>22.5	23.22 ± 0.62	⋯	1.3
ES-037	177.37796	22.35166	MACS1149	>26.3	24.19 ± 0.11	23.80 ± 0.11	⋯	1.1
ES-038[d]	181.53986	−8.82001	MACS1206	>26.3	23.39 ± 0.11	23.08 ± 0.06	0.51 ± 0.14	1.5
ES-039[e]	203.19160	50.55703	A1758	>26.6	22.51 ± 0.14	21.93 ± 0.07	⋯	1.8
ES-040[d]	203.20486	50.54511	A1758	>26.7	23.56 ± 0.12	23.09 ± 0.07	⋯	2.0
ES-041	228.73633	−15.39844	MACSJ1514.9–1523	>26.0	22.96 ± 0.41	22.36 ± 0.22	⋯	⋯
ES-042	228.75739	−15.38939	MACSJ1514.9–1523	>26.5	22.71 ± 0.13	22.49 ± 0.09	⋯	⋯
ES-043	292.95038	−26.57872	MACS1931	>26.4	20.88 ± 0.05	20.52 ± 0.04	0.45 ± 0.06	6.8
ES-044	310.81604	−21.74442	RXCJ2043.2–2144	>26.2	23.44 ± 0.36	22.22 ± 0.14	⋯	⋯
ES-045[d]	322.33627	−7.69648	MACS2129	>26.4	24.24 ± 0.25	23.64 ± 0.14	⋯	2.4
ES-046[d]	322.36267	−7.71412	MACS2129	>26.3	24.51 ± 0.23	23.87 ± 0.11	⋯	1.4
ES-047[d]	325.08832	−23.65191	MS2137	>26.3	22.62 ± 0.06	22.05 ± 0.04	⋯	1.4
ES-048	340.83810	−9.58147	MACSJ2243.3–0935	>26.1	23.20 ± 0.15	22.81 ± 0.14	⋯	⋯
ES-049[d]	342.15656	−44.56572	AS1063	>26.1	22.34 ± 0.03	22.08 ± 0.03	0.38 ± 0.13	1.3
ES-050	342.16800	−44.48981	AS1063	>25.7	21.47 ± 0.03	21.16 ± 0.02	⋯	1.1
ES-051[d]	342.22214	−44.57252	AS1063	>26.0	23.67 ± 0.07	23.27 ± 0.06	⋯	1.1
ES-052[d]	347.09330	−2.21299	A2537	>26.2	22.68 ± 0.06	22.20 ± 0.03	⋯	2.3
ES-053[d]	347.11108	−2.17515	A2537	>26.0	23.26 ± 0.07	22.60 ± 0.05	⋯	1.9

Notes. ES-006/07/08, ES-018/19, ES-028/29, and ES-045/46 are multiply imaged systems. ES-036 has a large uncertainty of CH2 magnitude (23.22 ± 0.62) because of a steep background brightness slope (and therefore large uncertainty) contributed by neighboring bright sources. The magnitude modeled with GALFIT is 23.45 ± 0.16.

[a] 5σ limit of F160W magnitude assuming point-source profile. If the source is extended, the actual magnitude limit could be higher by ∼0.5 mag (assuming $R_{e,circ} = 0\farcs25$, $b/a = 0.4$) to 1.2 mag (assuming $R_{e,circ} = 0\farcs45$, $b/a = 0.2$; see Section 3.1).

[b] Circularized effective radius measured in the IRAC CH2 band with GALFIT (Section 3.2).

[c] Lensing magnification factor (Section 4.2).

[d] Undetected ($<4\sigma$) in the MIPS 24 μm band. The typical 4σ upper limit is 61 μJy.

[e] Detected ($>4\sigma$) in the MIPS 24 μm band. The measured MIPS 24 μm flux densities are 46 ± 8 μJy (ES-005), 279 ± 29 μJy (ES-009) 263 ± 11 μJy (ES-028), 134 ± 15 μJy (ES-029) and 67 ± 11 μJy (ES-039).

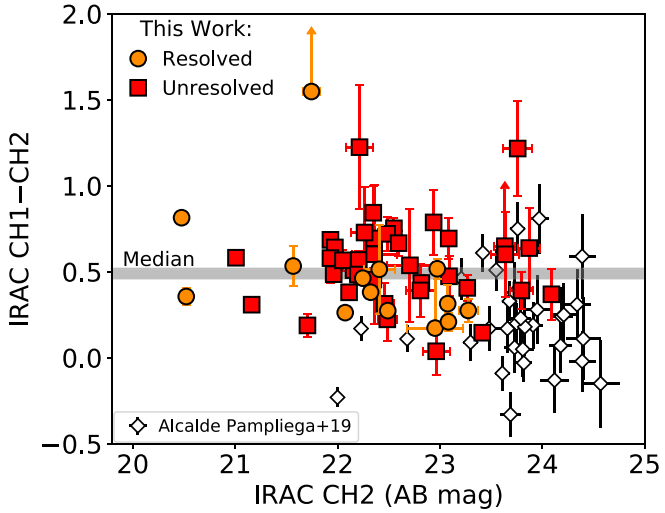

Figure 2. IRAC CH1−CH2 color vs. observed CH2 magnitude for resolved sources (orange circles) and unresolved sources (red squares). *H*-faint galaxies selected in the CANDELS/GOODS fields ($H_{160} \gtrsim 27.3$; Alcalde Pampliega et al. 2019) are shown as empty diamonds for comparison. The median IRAC CH1–CH2 color (0.49 ± 0.03) is indicated by the horizontal gray solid line.

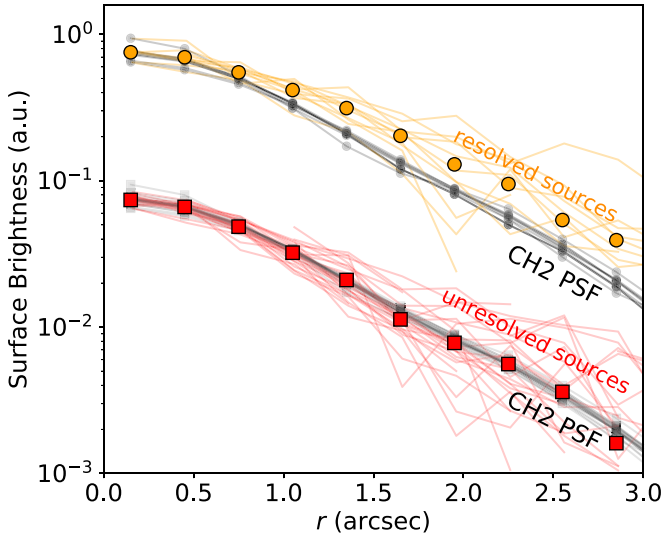

Figure 3. Radial surface brightness profiles of resolved (top; orange lines) and unresolved sources (bottom; red lines) in the IRAC CH2 band in arbitrary units (a.u.). All profiles are normalized by the peak brightness derived with a Gaussian fit, but we displace the two groups vertically by a factor of 10 for clarity. Radial profiles of the IRAC CH2 PSFs, constructed from the same fields of the *H*-faint sources, are shown as reference in black lines. The stacked radial profiles of resolved and unresolved sources are indicated by orange circles and red squares, respectively.

0.″6 aperture. We have also confirmed that 70% of the sources remain undetected even if we lower the detection threshold from 5 to 3σ. These indicate that our sample of *H*-faint galaxies is sufficiently robust against the choice of photometric aperture and detection threshold.

Owing to lensing magnification, sources in this sample are brighter than the *H*-faint galaxies in Wang et al. (2019) and Alcalde Pampliega et al. (2019) by ∼0.9 and 1.3 mag at 4.5 μm, respectively. All of the sources show red $H_{160} - \mathrm{CH2}$ colors of >2.5 (median $H_{160} - \mathrm{CH2} > 3.9$), consistent with those of the *H*-faint sources selected in CANDELS field (Caputi et al. 2012; Wang et al. 2019). We note that such $H_{160} - \mathrm{CH2}$ colors are calculated assuming point-source model, and extended source model assumption ($R_{\mathrm{e,circ}} \simeq 0.''25 - 0.''45$) will lead to bluer colors by ∼0.5 mag. As shown in Figure 2, the median IRAC CH1–CH2 color is 0.49 ± 0.03, suggesting a reddened stellar continuum in the IRAC bands or the presence of strong emission lines (Alcalde Pampliega et al. 2019). Given the $H - \mathrm{CH2}$ colors, brown dwarfs with a spectral type cooler than T7 may contaminate our sample (e.g., Kirkpatrick et al. 2021). However, the CH1 − CH2 colors of these brown dwarfs are very red (>1.2), and the only source with such a secure red CH1 − CH2 color in our sample (ES-031) can be resolved with IRAC CH2. Two sources (ES-022/44) tentatively fall in such a red CH1 − CH2 color range of brown dwarf, and we cannot rule out the possibility of such a contamination. However, the derived physical properties of overall sample will not change even if these sources are excluded.

Among 18 sources for which the IRAC CH3/CH4 data exist, we find that seven ($39\% \pm 11\%$) and eight ($44\% \pm 12\%$) sources can be detected at S/N > 4 at 5.8 μm and 8.0 μm using an $r = 2.''4$ aperture. We further measured the MIPS 24 μm flux densities of 21 sources for which the data exist. Among them, five sources can be extracted at S/N > 4 using $r = 3.''5$ aperture with an aperture-correction factor of 2.80, further discussed in Section 3.3. A similar fraction of MIPS-detected sources is also reported for the *H*-faint galaxy sample in Alcalde Pampliega et al. (2019). The typical 4σ upper limit of flux densities at 24 μm is 61 μJy.

For 30 sources with existing PACS data, we obtained photometric measurements with $r = 4''$ and $8''$ apertures at 100 and 160 μm. ES-009, ES-027, and ES-028 are the only sources extracted at S/N > 4 in at least one band. The typical 4σ upper limit of flux densities is 2 mJy at 100 μm and 4 mJy at 160 μm.

SPIRE 250–500 μm flux densities of 21 sources with MIPS data were extracted using the 24 μm priors with XID+ (Hurley et al. 2017), and ES-009 is the only source detected at $>4\sigma$ in any SPIRE band, as further discussed in Section 3.3. The typical 4σ upper limit of SPIRE flux densities is 8–9 mJy in all three bands.

3.2. Profile Modeling

We further modeled the IRAC/CH2 surface brightness profiles of all 53 sources using GALFIT (Peng et al. 2010). We only modeled their profiles in the CH2 maps instead of the CH1 maps because (i) the full widths at half maximum (FWHMs) of IRAC PSFs in CH1 and CH2 are similar and (ii) the S/N in CH2 is higher than that in CH1. Sun et al. (2021) demonstrate that IRAC can resolve the lensed stellar continua of dusty star-forming galaxies at $z \sim 2$ in the rest-frame *J* and *H* bands. At a source redshift of $z = 4$ and a lensing magnification factor of $\mu = 2$, IRAC would be able to resolve a source with a circularized effective radius greater than ∼2 kpc.

We first constructed the CH2 PSF models from the stars in the mosaic images of all the cluster fields using a PHOTUTILS routine (Bradley et al. 2020). These PSF kernels were then used by GALFIT for model convolution. We then extracted a catalog of neighboring field sources from F160W images, and the positions and profile parameters (semimajor axis, axis ratio, positional angle) were then used as prior information for the profile modeling in CH2. We tried both the Sérsic and point-source models for the *H*-faint sources, and the final adopted models represent fittings with a higher quality (lower χ^2 or more reasonable parameters, e.g., Sérsic index $n \lesssim 4$).

Fourteen out of the 53 *H*-faint sources are spatially resolved in the IRAC/CH2 band. The radial surface brightness profiles of resolved and unresolved sources are displayed in Figure 3 separately. We derived a mean Sérsic index of $n_{\mathrm{mean}} = 0.8 \pm 0.1$ (typical uncertainty for individual sources is 0.6). This is consistent

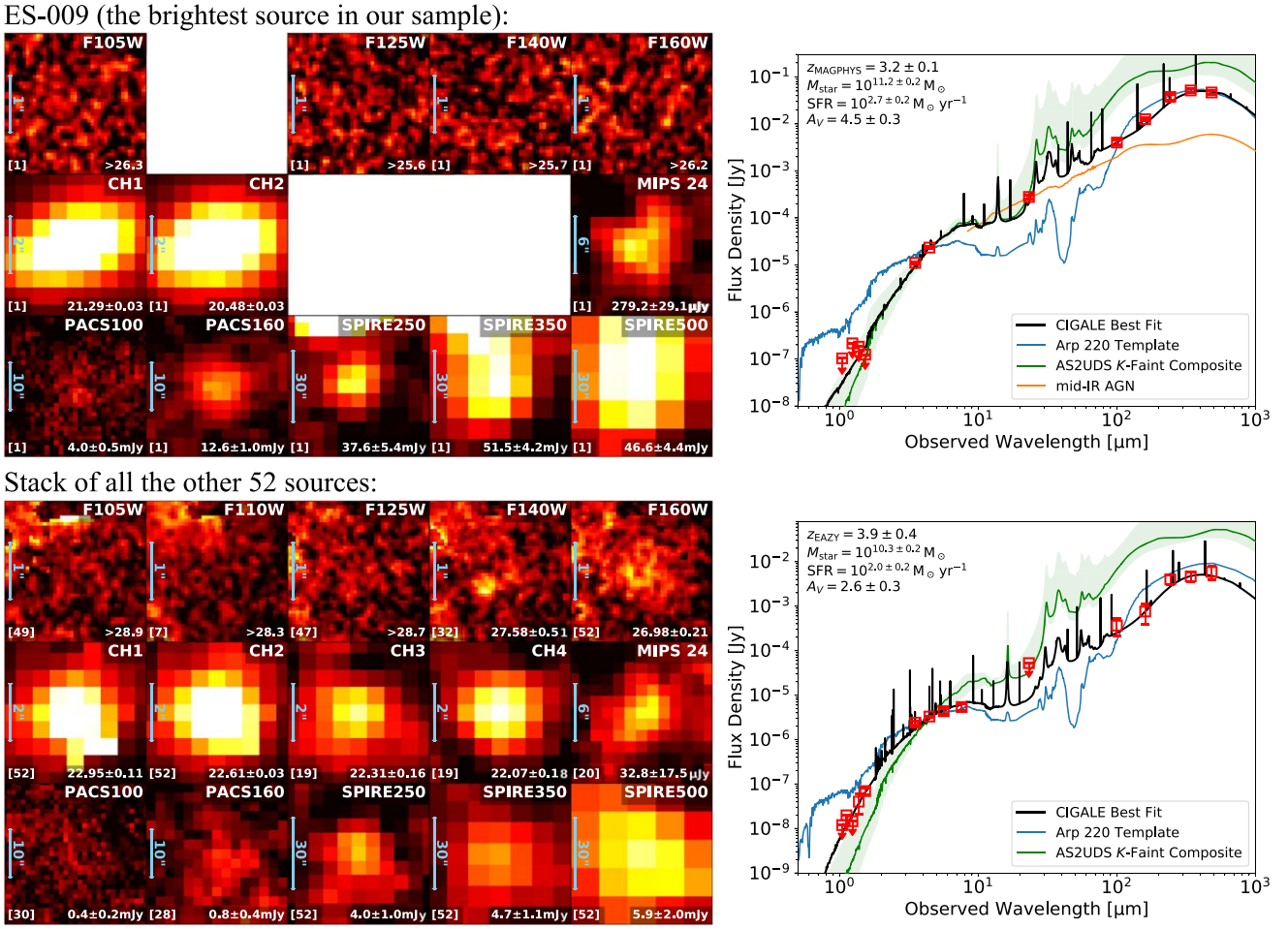

Figure 4. Top left: cutout images of ES-009, the brightest source in our sample, from the near-IR to far-IR. In each image, the band name is indicated at the upper-right corner, and the measured brightness is noted at the lower-right corner (in AB magnitude if $\lambda \leqslant 8$ μm, and in flux density if $\lambda > 8$ μm). Numbers in brackets at the lower-left corners are the numbers of images stacked (one for ES-009). Scale bars of various lengths are plotted in the left of the cutout images. Top right: best-fit SED of ES-009 obtained with CIGALE (the black solid line). The photometric data are plotted as open red squares. For comparison, we also plot the SED templates of Arp 220 (ULIRG; the blue line), mid-IR AGN (Kirkpatrick et al. 2015; the orange line), and AS2UDS *K*-faint SMGs (Smail et al. 2021; the green line with shaded region for the 16–50–84th percentiles of the distribution). All the templates are redshifted to the same z_{phot} of ES-009 and normalized to the source flux density at 4.5 μm, except for the AGN template, which is normalized to the 24 μm flux density. Derived physical properties with CIGALE (M_{star}, SFR, and A_V; lensing magnification corrected) are noted at the upper-left corner. Bottom: stacked images of all the other 52 sources in the sample (left) and the best-fit SED obtained with CIGALE (right). The layouts are the same as those of the top panels.

with the average Sérsic index ($n \sim 1$) of the stellar continua of SMGs at $z \sim 2$ measured in either the F160W band (unlensed sample; e.g., Chen et al. 2015; Fujimoto et al. 2018; Lang et al. 2019) or IRAC bands (lensed sample; Sun et al. 2021). Most of the resolved sources show an elongated shape in the IRAC CH2 (mean axis ratio $b/a = 0.20 \pm 0.05$), reflecting a strongly lensed nature or presence of a multiple-component structure. The GALFIT-derived magnitudes are also consistent with the aperture-photometry magnitudes (median difference is 0.04 ± 0.03 mag), suggesting that the source blending will only have a limited influence on the aperture-photometry measurements.

For the resolved sources, we report their circularized effective radii ($R_{e,circ}$) in Table 2. The mean $R_{e,circ}$ of the 14 resolved sources is $0\farcs46 \pm 0\farcs04$. We also derived the $R_{e,\ circ}$ using the 1D radial surface brightness profiles of these 14 sources. Through a Gaussian fitting of the radial profiles of *H*-faint sources and corresponding PSF models, we deconvolved the Gaussian rms widths of the sources by those of the PSFs and derived the circularized effective radii $R^{1D}_{e,circ}$. The mean ratio between the effective radii measured on 2D maps (GALFIT) and 1D profiles is $R_{e,circ}/R^{1D}_{e,circ} = 0.9 \pm 0.1$, suggesting a good consistency.

3.3. Notable Sources

Among the 53 *H*-faint galaxies, we have identified a few notable sources for which we obtained further measurements. We describe these sources here.

3.3.1 ES-009

This source is the brightest (CH2 = 20.48 ± 0.03 mag) *H*-faint source found in our sample (Figure 4). It is also brighter than any *H*-faint source found in the CANDELS fields (the brightest is at CH2 = 21.96; Wang et al. 2019), any $K > 25.3$ SMG reported in the UDS field (the brightest is at CH2 = 22.24; Smail et al. 2021; Dudzevičiūtė et al. 2020), and any optical/near-IR-dark ALESS SMGs reported in the ECDFS field (the brightest is at CH2 = 22.27; Simpson et al. 2014). Stacking the four-band HST data (F105W, F125W, F140W, and F160W) of this source yields no detection. Furthermore, we detected the IR counterpart of this source in the MIPS 24 μm and all the five Herschel bands (100–500 μm; see Figure 4). According to the mid-IR active galactic nucleus (AGN) template by Kirkpatrick et al. (2015), the AGN

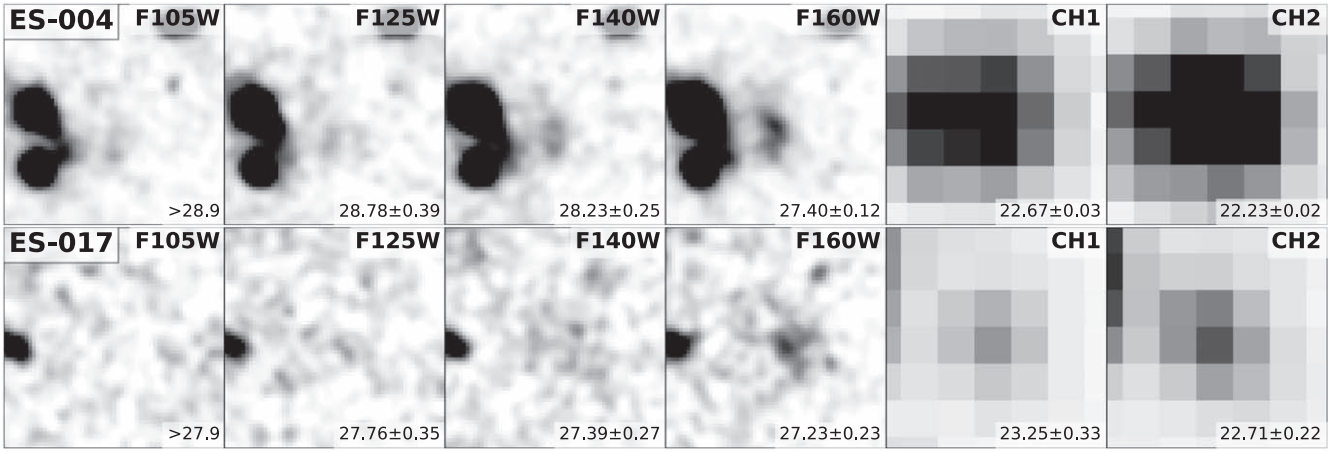

Figure 5. Deep cutout images of ES-004 (in A2744) and ES-017 (in MACS0416). Here the displayed HST images are HFF data (Lotz et al. 2017), which are deeper than those of BUFFALO and other fields by about four times (in terms of rms noise). HST images are smoothed with a Gaussian kernel (FWHM = 0.″2). The band name of each image is indicated at the upper-right corner, and the source magnitude is shown at the lower-right corner. The magnitude limits are at 3σ. The size of each cutout image is $3.''6 \times 3.''6$.

contribution to its far-IR SED should be less than 10%. The far-IR continuum of this source peaks around 350 μm ($S_{350} = 52 \pm 4$ mJy), suggesting a likely redshift solution of $z \sim 3$.

3.3.2 ES-005, ES-028, ES-029, ES-039

Among all the 21 sources that were observed with the Spitzer/MIPS at 24 μm (Table 2), these four sources together with ES-009 are the only cases that are detected in the MIPS 24 μm band. The measured MIPS 24 μm flux densities are 46 ± 8 μJy (ES-005), 263 ± 11 μJy (ES-028), 134 ± 15 μJy (ES-029), and 67 ± 11 μJy (ES-039). If these sources reside at $z > 3$, then the MIPS detections may imply the presence of hot dust component dominated by AGN (see Wang et al. 2016; Alcalde Pampliega et al. 2019), and if that is the case, the determination of their photometric redshifts and stellar masses may be inaccurate.

3.3.3 ES-004, ES-017

These two sources are located in the coverage of the original HFF data. We therefore conducted aperture photometry using the deep HFF data in the WFC3-IR F105W, F125W, F140W, and F160W bands with the same method described in Section 3.1. With the HFF data, whose rms noise is only ~25% of the median rms noise of our sample, we securely detected ES-004 and ES-017 at 1.6 μm, and both sources are marginally detected at $\lambda_{\rm obs} \gtrsim 1$ μm (Figure 5). These two sources are not special from the others in terms of intrinsic physical properties.

3.4. Stacking

We conducted stacking analysis to constrain the spectral energy distributions (SEDs) of the *H*-faint sources. This is because the studies on the intrinsic properties of individual sources are hampered by the non-detections in the HST and Herschel bands. We split the sources into subsamples by their observed properties. These groups are (i) all the 52 sources except for ES-009, which is firmly detected in all the available bands at $\lambda \geqslant 3.6$ μm, (ii) four sources (ES-005, ES-028, ES-029, and ES-039) that are detected at 24 μm (hereafter MIPS-bright sample), (iii) 16 sources that are undetected at 24 μm (hereafter MIPS-faint sample), (iv) 13 resolved sources excluding ES-009, and (v) 39 unresolved sources.

For sources within each group, we stacked their images in each band with inverse variance weighting of the images. Similar to Wang et al. (2019), we first normalized all the images by the IRAC CH2 flux densities of the sources, and then multiplied the resulting fluxes of stacked source with the median IRAC CH2 flux density. To mitigate the effect of source confusion in the Herschel bands, where the angular resolution is coarse, the images that we stacked are residual images from which nearby sources are removed. In these images, we first identified Herschel sources with the DAOFIND routine (Stetson 1987), and then subtracted all the S/N > 3 sources that are at least one-half beam FWHM away from any *H*-faint source of interest using the PSF models.

We note that we used the BUFFALO-only HST data of ES-004 and ES-017 for the stacking of HST images, instead of the deep HFF data shown in Figure 5. This is because, with the inverse variance weighting, the weight of deep HFF images are ~16 times that of the others, and thus these two sources would dominate the signal in the final stack.

We measured the flux densities of the stacked sources with aperture photometry. We adopted aperture sizes of $r = 0.''6$ in all the HST bands, $1.''8$ in the IRAC CH1/2, $2.''4$ in the IRAC CH3/4, $7''$ in the MIPS 24 μm, and $5''$, $10''$, $18''$, $27''$, and $36''$ at 100–500 μm. Aperture-correction factors were calculated based on PSF models for all Spitzer and Herschel bands, and photometric uncertainties were first calculated from the rms of the stacked background. For aperture corrections in the HST bands, we assumed an exponential source profile with $R_{\rm e,circ} = 0.''25$. For ES-009 and the stack of the IRAC-resolved sources, we assumed the $R_{\rm e,circ} = 0.''45$ model. These assumptions were to address the extended source profile and potential smearing effect because of the astrometric uncertainty. If the source is detected at S/N > 3 in the stacked image, we evaluate the uncertainty with bootstrapping (same method as Schreiber et al. 2015 and Wang et al. 2019 for the stacking in the Herschel bands). Therefore, the derived flux density uncertainties incorporate the intrinsic dispersion of sources stacked. Table 3 presents the photometric properties of the stacked sources.

Table 3
Properties of *H*-faint Galaxies

Parameters	Individual ES-009	Stacked[a]		
		All (52)	MIPS-faint (16)	MIPS-bright (4)
		Photometric Properties[b]		
WFC3-IR/F105W (mag)	>26.3	>28.7	>28.1	>27.5
WFC3-IR/F110W (mag)	···	>28.2	>27.0	>26.1
WFC3-IR/F125W (mag)	>25.6	>28.5	>27.9	>26.1
WFC3-IR/F140W (mag)	>25.7	>27.0	>25.8	>26.7
WFC3-IR/F160W (mag)	>26.2	26.79 ± 0.21	26.38 ± 0.19	26.52 ± 0.23
IRAC/CH1 (mag)	21.29 ± 0.03	22.95 ± 0.11	23.25 ± 0.06	22.79 ± 0.07
IRAC/CH2 (mag)	20.48 ± 0.03	22.61 ± 0.03	22.77 ± 0.02	22.14 ± 0.04
IRAC/CH3 (mag)	···	22.31 ± 0.16	22.92 ± 0.18	21.78 ± 0.14
IRAC/CH4 (mag)	···	22.07 ± 0.18	22.34 ± 0.32	21.86 ± 0.16
MIPS 24 μm (mJy)	0.28 ± 0.03	0.03 ± 0.02	<0.02	0.13 ± 0.01
PACS 100 μm (mJy)	4.0 ± 0.5	0.4 ± 0.2	<0.7	1.0 ± 0.2
PACS 160 μm (mJy)	12.6 ± 1.0	0.8 ± 0.4	<1.4	2.3 ± 0.8
SPIRE 250 μm (mJy)	37.6 ± 5.4	4.0 ± 1.0	<4.8	7.3 ± 3.6
SPIRE 350 μm (mJy)	51.5 ± 4.2	4.7 ± 1.1	<4.7	7.1 ± 3.3
SPIRE 500 μm (mJy)	46.6 ± 4.4	5.9 ± 2.0	7.6 ± 3.0	<12.3
		Physical Properties[c]		
$z_{\rm EAZY}$	···	$3.9^{+0.4}_{-0.4}$	$3.6^{+0.4}_{-0.3}$	$2.6^{+0.4}_{-0.4}$
$z_{\rm MAGPHYS}$	$3.2^{+0.1}_{-0.1}$	$2.7^{+1.0}_{-0.4}$	$3.2^{+0.6}_{-0.6}$	$1.8^{+0.3}_{-0.2}$
μ	3.3	2.2	2.0	2.2
A_V	4.5 ± 0.3	2.6 ± 0.3	2.3 ± 0.3	4.0 ± 0.6
$\log[M_{\rm star}/(M_\odot)]$	11.2 ± 0.2	10.3 ± 0.2	10.1 ± 0.2	10.2 ± 0.2
$\log[L_{\rm IR}/(L_\odot)]$	12.8 ± 0.2	12.0 ± 0.2	11.8 ± 0.2	11.9 ± 0.3
$\log[{\rm SFR}/(M_\odot\ {\rm yr}^{-1})]$	2.7 ± 0.2	2.0 ± 0.2	1.7 ± 0.2	1.9 ± 0.3

Notes.
[a] From left to right: stack of all 52 sources except for ES-009; 16 sources that are undetected at 24 μm; four sources (ES-005, ES-028, ES-029, and ES-039) that are detected at 24 μm.
[b] Normalized by the median IRAC/CH2 flux densities (Section 3.4). Upper limits are at 3σ.
[c] A_V, $M_{\rm star}$, $L_{\rm IR}$, and SFR are derived with CIGALE (Section 4.3). Lensing magnification is corrected for $M_{\rm star}$, $L_{\rm IR}$, and SFR.

Figure 4 shows the stacked images of the 52 sources in all 15 bands. The stacked source can be firmly detected in the majority of the bands, except for non-detections in the WFC3-IR/F105W, F110W, F125W, and marginal detections in the WFC3-IR/F140W and PACS 100 μm bands. The stellar continuum of the stacked source peaks around IRAC/CH4 and the dust continuum peaks around SPIRE 500 μm, both favoring a redshift solution around $z \sim 4$. Although the stacked source is firmly detected at 24 μm, the large uncertainty of flux density suggests that the MIPS flux can be contributed and biased by a few MIPS-bright sources. Further stacking analysis of the 16 MIPS-faint sources suggests a 3σ upper limit of <17 μJy at 24 μm with a median CH2 magnitude of 22.8. Such a flux density can be more than seven times lower than that of the MIPS-bright sources (127 ± 12 μJy).

Because the far-IR flux densities of *H*-faint sources may not correlate well with those measured in the IRAC/CH2 band (e.g., Wang et al. 2019), we also tried to stack images without any normalization. The derived photometric results show general consistency with the CH2-normalized results within an $\sim 1\sigma$ confidence interval. Similar consistency can also be found if we adopt median stacking instead of the inverse variance method.

One well-known caveat for stacking the measurements of a likely mixed population is that the derived physical properties can still deviate from the average properties of individual sources. Stacking sources in a wide redshift range can lead to an artificial broadening of spectral features. Additionally, if the *H*-faint sample comprises both dusty star-forming galaxies and old passive systems (i.e., below the 1σ dispersion of the star-forming main sequence as shown in Wang et al. 2019, and thus likely at slightly lower redshifts), then the stacked SEDs may be biased toward the passive population with less dust obscuration in the near/mid-IR but dominated by the active population in the far-IR. Further constraints on the far-IR luminosities with ALMA or NOEMA observations will be able to decompose such a mixed population by allowing accurate SFR measurements of individual sources.

4. Analysis and Discussion

4.1. Photometric Redshift

With the SEDs described in Sections 3.3 and 3.4 through direct photometry (ES-004, ES-009, and ES-017) and stacking, we run SED modeling software to derive the photometric redshift (photo z, $z_{\rm phot}$) of the *H*-faint sources. We do not model the SEDs of the majority of individual sources because most of them are only detected in two IRAC bands, and the constraints on the dust continua are poor. The lensing magnifications are only corrected for physical quantities after SED fitting, and therefore do not enter the calculation of photometric redshifts.

We first estimate the $z_{\rm phot}$ using the nine-band near/mid-IR ($\lambda \leqslant 8$ μm) SEDs with EAZY (Brammer et al. 2008). Similar to Wang et al. (2019), we use the full set of spectral template library allowing A_V up to 5. The best-fit $z_{\rm phot}$ of the stacked 52

sources (excluding ES-009) derived with EAZY is 3.9 ± 0.4 (uncertainty denotes the 16–84th percentiles of the likelihood distribution), consistent with the median photometric redshift of *H*-faint sources reported in the CANDELS fields ($z_{\rm phot,med} = 3.9 \pm 0.1$; Wang et al. 2019), ALESS optically faint SMGs (3.7 ± 0.1; da Cunha et al. 2015), *K*-faint AS2UDS SMGs (3.5 ± 0.1 for the subset studied in Smail et al. 2021), serendipitous *H*-faint sources detected with the GOODS-ALMA survey ($\sim$3.5; Franco et al. 2018, 2020; Zhou et al. 2020), and the ALMA large program ALPINE ($\sim$3.7; Gruppioni et al. 2020), as well as the broad redshift range of $z = 3 \sim 5$ suggested by Yamaguchi et al. (2019) based on the IRAC–ALMA and ALMA–JVLA flux ratios. This is smaller than the median redshift (4.8) for the sample of Alcalde Pampliega et al. (2019), in which the sources are intrinsically fainter (down to CH2 = 24.5). The derived photo z's of ES-004 ($4.1^{+0.6}_{-1.7}$), ES-017 ($3.7^{+1.2}_{-1.0}$), the stack of the IRAC-unresolved sources ($3.9^{+0.9}_{-0.8}$), IRAC-resolved sources ($2.6^{+1.4}_{-0.4}$), and MIPS-faint sources ($3.6^{+0.4}_{-0.3}$) are consistent with that of the stack of 52 sources, but MIPS-bright sources are likely at a lower redshift (2.6 ± 0.4). The best-fit model of ES-009 suggests unreasonable redshift at $z \sim 7$ because it is only detected in the IRAC CH1/2 bands (CH3/4 data do not exist).

We also estimate the $z_{\rm phot}$ and derive the physical properties simultaneously using the full near-to-far-IR SEDs with MAGPHYS+PHOTOZ (da Cunha et al. 2008; Battisti et al. 2019). MAGPHYS is an energy-balance SED modeling software which assumes a continuous delayed exponential star formation history (SFH) with random starburst and a two-component dust absorption law (i.e., diffuse ISM and stellar birth cloud; Charlot & Fall 2000). This is the extension of the software that da Cunha et al. (2015) used for the analysis of optically faint ALESS SMGs reported in Simpson et al. (2014) and Smail et al. (2021) used it for the analysis of *K*-faint SMGs in the UDS field (AS2UDS sample; Stach et al. 2019; Dudzevičiūtė et al. 2020). Note that we adopt a uniform prior distribution of redshift instead of the default one that peaks at $z \sim 2$ (Battisti et al. 2019).

The best-fit MAGPHYS $z_{\rm phot}$ for the stack of the 52-source sample is $2.7^{+1.0}_{-0.4}$ (uncertainty denotes the 16–84th percentiles of the likelihood distribution). The large uncertainty on the derived $z_{\rm phot}$ may imply an intrinsically broad redshift distribution of *H*-faint galaxies (likely $z \simeq 2$–5). This is supported by the redshift distribution of individual sources seen in Wang et al. (2019) and Gruppioni et al. (2020). We also derive the photometric redshift for ES-009 (3.2 ± 0.1) and the stack of the MIPS-bright ($1.8^{+0.3}_{-0.2}$) and MIPS-faint sample (3.2 ± 0.6), respectively. The redshifts derived with MAGPHYS are generally lower but marginally consistent with those obtained with EAZY. We conclude that the majority of *H*-faint galaxies selected in this work are at similar median redshifts ($z_{\rm med} \simeq 3.5$–4) reported in previous studies, although a small fraction of them can be located at a lower redshift of $z \simeq 2$–3.

4.2. Lens Models and Magnification

We utilize published cluster lens models to infer the lensing magnification and thus the intrinsic physical properties. These are available for 24 out of the 32 clusters, including six HFF clusters, six CLASH clusters, and 12 RELICS clusters. For sources detected in the HFFs, we use the lens models produced by the CATS team (Jauzac et al. 2014, 2015, 2016; Limousin et al. 2016; Mahler et al. 2018; Lagattuta et al. 2019) because of a larger field coverage at a high resolution (0.″2). We also use the large-area low-resolution lens model produced by Merten et al. (2011) in MACS0416 and MACS1149, where the identified sources are out of the coverage of the CATS products. For sources detected in the CLASH and RELICS cluster fields, we use all of the available lens models on the MAST high-level science product database, including those produced by CATS (Richard et al. 2014), Zitrin-dPIEeNFW and Light-Traces-Mass (Zitrin et al. 2013, 2015), and GLAFIC (Oguri 2010; Kawamata et al. 2016; Okabe et al. 2020).

We assume a point-source model for the extraction of magnification factor (μ). Based on the photometric redshifts presented in Section 4.1, we estimate the lensing magnifications for most of the sources at $z = 4$. The magnifications for the four MIPS-bright sources are estimated assuming $z = 2.6$, and for ES-009 we assume $z = 3.2$. If multiple lens models are available for the same source, we adopt the geometric mean of all magnifications. As summarized in Table 2, lensing magnifications are available for 42 sources in our sample. In Appendix A, we show the magnifications versus distances to cluster center of these sources as the top-right panel of Figure 10. Only two sources are found at $\mu > 5$, indicating that lensing-boosted rest-frame UV-optical offset of high-redshift dusty galaxies (e.g., Fujimoto et al. 2016) is not the cause of non-detection in the F160W band. We also note that we may preferentially miss strong galaxy-galaxy lensed objects because of a selection bias against sources within 1″ of the foreground lens.

The 16th, 50th, and 84th percentiles of the magnification distribution are 1.3, 2.2, and 3.0. We uniformly assume $\mu_{\rm med} = 2.2$ for 11 sources without available lens models. This is also consistent with the median magnification of sources at comparable distances to the cluster centers ($r = 0.″9^{+0.3}_{-0.4}$). For each individual source with available lens models, we estimate a typical magnification uncertainty of $\sigma_\mu/\mu \sim 20\%$ based on the standard deviation of magnifications predicted by different models. The magnification uncertainty introduced by the redshift uncertainty (i.e., $\sigma_z/(1+z) \sim 20\%$) is found to be a minor effect ($\sigma_\mu/\mu \sim 5\%$ at $\mu_{\rm med} = 2.2$).

With these lens models, four multiply lensed systems can be identified in our sample, including ES-006/07/08 (in MACSJ0032.1+1808), ES-018/19 (in MACSJ0417.5-1154), ES-028/29 (in A697), and ES-045/46 (in MACS2129). This further reduces the number of independent sources in our sample to 48.

4.3. Statistics of Physical Properties

We find that MAGPHYS derives an abnormally low ratio of $\rm SFR/L_{IR}$ ($10^{-10.6}\,M_\odot\,{\rm yr}^{-1}\,{\rm L}_\odot^{-1}$) for all of the *H*-faint source groups. This is only one-third of that observed for optically faint SMGs at similar redshifts ($10^{-10.1}\,M_\odot\,{\rm yr}^{-1}\,{\rm L}_\odot^{-1}$; e.g., da Cunha et al. 2015; Smail et al. 2021) and the Kennicutt (1998) conversion factor assuming a Chabrier IMF, which is likely caused by a large contribution of diffuse dust emission to $L_{\rm IR}$ as assumed by MAGPHYS. To address this issue, we further model the SEDs with the energy-balance code CIGALE (Noll et al. 2009; Boquien et al. 2019) assuming a continuous delayed SFH with a recent starburst in the past 20 Myr. This is to interpret the dust and reddened stellar continuum simultaneously with a dusty starburst and an old population. We also assume a modified Calzetti et al. (2000) extinction law (allowing a steeper power-law slope index up to 0.4; see

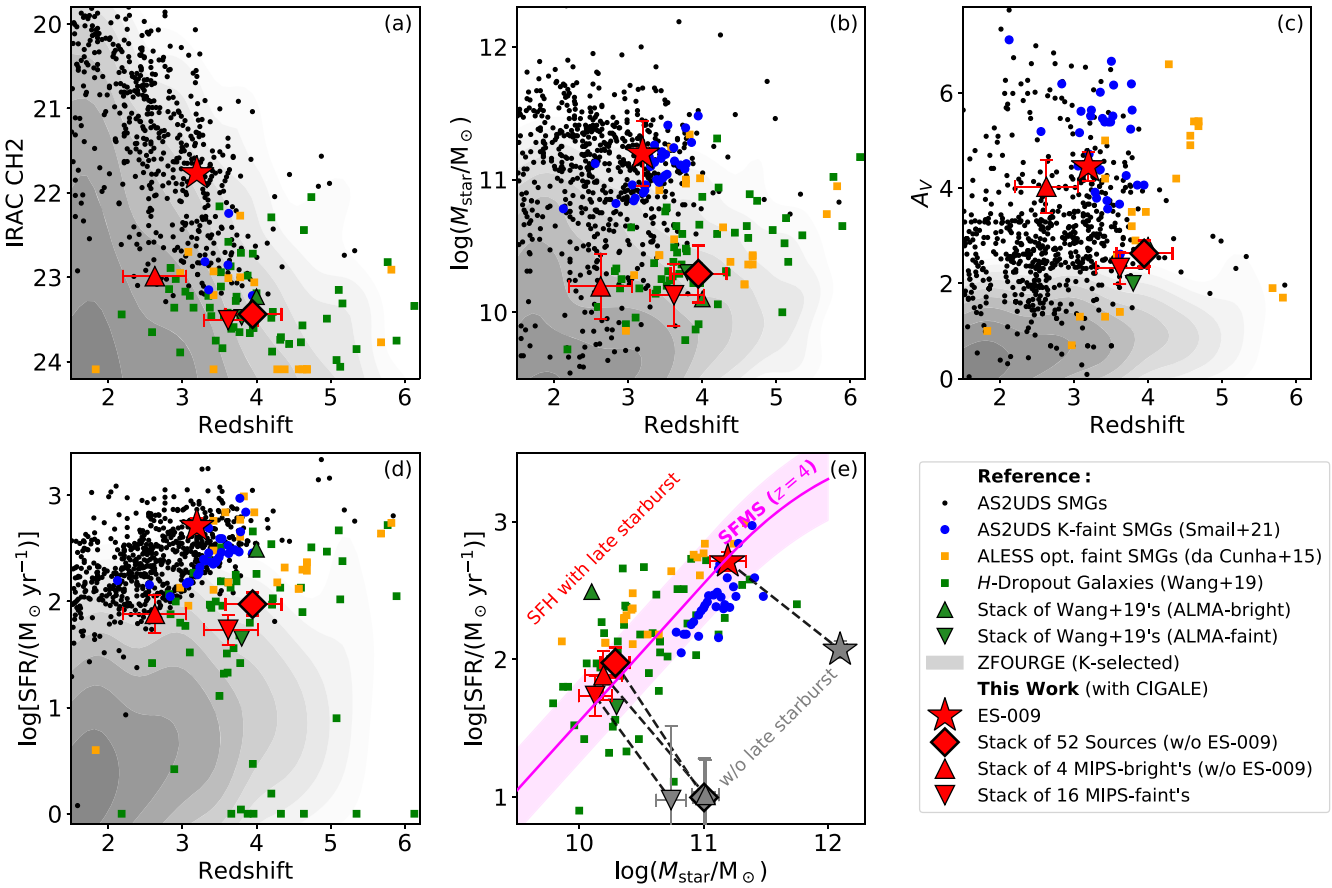

Figure 6. Physical properties of *H*-faint galaxies (from panel (a) to (d): IRAC CH2 magnitude, stellar mass, rest-frame *V*-band attenuation, SFR vs. redshift; panel (e): SFR vs. stellar mass). Lensing magnification has been corrected. Sources in our sample are shown as red symbols with black edges in all panels, including ES-009 (star), stack of the other 52 sources (diamond), stack of the MIPS-bright sources (upward triangle), and MIPS-faint sources (downward triangle). Reference samples include (i) submillimeter-selected AS2UDS SMGs (black dots; Dudzevičiūtė et al. 2020), AS2UDS SMGs at $K > 25.3$ (blue circles; Smail et al. 2021), optically faint ALESS SMGs (orange squares; Simpson et al. 2014; da Cunha et al. 2015), (ii) IRAC-selected *H*-faint galaxies in CANDELS fields (green squares for individual sources, upward/downward triangles for the stacks of ALMA-detected/undetected sources; Wang et al. 2019), and (iii) *K*-band-selected ZFOURGE galaxies (gray contours in the background at arbitrary levels; Straatman et al. 2016). In panel (e), we also plot the star-forming main sequence and its 1σ dispersion at $z = 4$ (magenta solid line; Schreiber et al. 2015). The differences between the $M_{\rm star}$ and SFR derived with CIGALE (with a late starburst in the SFH; red-filled symbols) and MAGPHYS (without mandatory late starburst; gray-filled symbols) are indicated by the black dashed lines.

Salim & Narayanan 2020), and nebular emission is included in the modeling. We use EAZY-derived $z_{\rm phot}$ for all the cases except for ES-009, where the MAGPHYS-derived model is adopted. We run Monte-Carlo sampling of photometric redshifts based on their probability distributions and then feed into the CIGALE fitting routine, and thus the uncertainties of derived physical properties incorporate the uncertainties of redshifts. We note that CIGALE is not designed as a photoz code. However, based on the χ^2_ν of best-fit SED models of the same source at different redshifts, we find that $\exp[-\chi^2_\nu(z)]$ can be well modeled with a Gaussian function peaking at the same $z_{\rm phot}$ as that derived with EAZY for most of the cases except for ES-009, whose probability function peaks around $z = 3.5$.

With CIGALE, we derive a median stellar mass of $10^{10.3\pm0.3}$ $M_\odot$, SFR of 100^{+60}_{-40} $M_\odot$ yr^{-1} and rest-frame *V*-band attenuation of $A_V = 2.6 \pm 0.3$ for the stacked 52 sources in our sample after correcting for the median magnification. Similar $M_{\rm star}$ and SFR are derived for the stacked MIPS-bright and MIPS-faint sources. However, we find that the MIPS-bright sources show a larger A_V (4.0 ± 0.6) over the MIPS-faint sample (2.3 ± 0.3), highlighting that the $H_{160} - {\rm CH2}$ selection technique is subject to a degeneracy of $z_{\rm phot} - A_V$ (also pointed out in Caputi et al. 2012; Wang et al. 2016). The brightest source ES-009 is found to host a stellar mass of $10^{11.2\pm0.2}$ $M_\odot$ and SFR of 500^{+290}_{-180} $M_\odot$ yr^{-1} with an A_V of 4.5 ± 0.3. A summary of physical properties can be found in Table 3.

Figure 6 shows the physical properties of optical/near-IR-dark galaxies presented in several works. We find that the assumption of SFH holds the key to the interpretation of $M_{\rm star}$ and SFR in *H*-faint galaxies. With the addition of the late starburst that can contribute $22\% \pm 9\%$ of the stellar mass in the CIGALE modeling, the derived SFR is 7 ± 1 times higher than that of MAGPHYS-derived one but $M_{\rm star}$ is 6 ± 1 times lower (see Figure 6(e)). We favor the CIGALE results because of a more commonly adopted SFR/$L_{\rm IR}$ ratio and a lower $M_{\rm star}$ that is compatible with the observed galaxy stellar mass function (SMF) at $z \sim 4$ (e.g., Muzzin et al. 2013; Song et al. 2016). Additionally, the measured Sérsic indices of resolved *H*-faint sources ($n \sim 0.8$) do not resemble those of quenching galaxies as indicated by MAGPHYS (i.e., $\gtrsim$10 times below the star-forming main sequence as shown in Figure 6(e); Schreiber et al. 2015).

We note that the goodness of fit with the two softwares are comparable ($\chi^2_\nu \sim 1$), and assuming the same extinction law (Charlot & Fall 2000) does not mitigate the conspicuous difference in either SFR or $M_{\rm star}$. Similarly, the SFR and $M_{\rm star}$

modeled with MAGPHYS (da Cunha et al. 2015; optimzed for high-redshift applications) using the same $z_{\rm phot}$ derived with EAZY are consistent with those derived with MAGPHYS +PHOTOZ instead of CIGALE.

Recent studies on massive galaxies at $z<1$ also suggest that parametric SFH modeling may underestimate the uncertainties of SFR and $M_{\rm star}$ when compared to those with nonparametric/stochastic SFH assumptions (e.g., Leja et al. 2019; Iyer et al. 2020), and it is possible that the true SFR and $M_{\rm star}$ of H-faint galaxies are between the CIGALE and MAGPHYS fitting results. This underscores the difficulty of physical property characterization with limited information in the optical/near-IR bands.

We also assess the impact of the late burst age on the SED modeling results. Assuming a 100 Myr late burst (i.e., $\sim$10% of the maximum age of these galaxies, which is consistent with their number density among the broader population; see Section 4.6), we find that with an $\sim$40% increase of mean χ^2_ν to $\sim$1.5, the derived SFR ($M_{\rm star}$) of all groups will slightly decrease (increase), but still within the 1σ uncertainties of those quantities derived with a 20 Myr late burst. Similarly, adopting lower $z_{\rm phot}$ derived with MAGPHYS will also lead to a small decline of estimated SFR and $M_{\rm star}$, which are also within the uncertainties summarized in Table 3. This further suggests that the uncertainties of derived physical properties of H-faint galaxies are dominated by systematic factors (e.g., assumption of SFH).

The stellar mass and A_V of H-faint sources in our sample are consistent with those reported by Wang et al. (2019) using the same software. The SFR of the stacked sources in our sample is between those of ALMA-detected and undetected H-faint galaxies in Wang et al. (2019), suggesting that the sample consists of galaxies across the wide dispersion of the so-called star-forming main sequence at $z\sim4$ ($\sigma\sim0.3$ dex; Schreiber et al. 2015). Compared with submillimeter-selected optical/near-IR-dark galaxies in da Cunha et al. (2015); Dudzevičiūtė et al. (2020) and Smail et al. (2021), sources in our sample are generally lower in SFR and A_V because 850 μm selection favors dust-rich galaxies with high SFR. A lower $M_{\rm star}$ is derived for our sample despite comparable 4.5 μm flux densities, and this can be interpreted by the difference in dust extinction and SFH assumption.

Assuming $z_{\rm phot}=3.9$ for the stack of 52 sources, we derive a dust temperature of 40 ± 6 K from a modified blackbody fit to the Herschel/SPIRE flux densities (dust emissivity $\beta=1.5$). We note that the Herschel data alone cannot provide a tight constraint on dust temperature because of rising SPIRE flux densities as a function of wavelength and the artificial broadening due to stacking. However, the derived $T_{\rm dust}$ is generally consistent with the $T_{\rm dust}$ of $L_{\rm IR}=10^{12}\,L_\odot$ galaxies at $z\simeq3-4$ as reported by (Schreiber et al. 2018a; $\sim$38 K), as well as the $T_{\rm dust}$ of stacked H-faint galaxies in (Wang et al. 2019; $\sim$37 K) assuming the same β.

4.4. Resolved Stellar Continuum

We find that the IRAC-resolved H-faint galaxies are generally at a higher lensing magnification ($\mu_{\rm med}=2.8\pm0.4$) than the unresolved sample ($\mu_{\rm med}=2.0\pm0.2$), which is likely a selection effect. After correcting the lensing magnification, we find no clear difference of stellar mass or SFR between the two samples.

Figure 7 shows the circularized effective radii versus stellar mass of H-faint galaxies in our sample. For those unresolved sources, we assume upper limits of their angular size at $R_{\rm e,circ}<0\farcs3\,\mu^{-0.5}$ (i.e., FWHM less than one pixel). Stellar mass of each source is computed using the IRAC/CH2 flux density assuming the same intrinsic SED of the stacked source. We adopt a conversion factor of $0.144\,''\,{\rm kpc}^{-1}$ from the angular to physical scale at $z=4$, which is insensitive to the variation of redshift. For the 14 resolved sources, we measured a median $R_{\rm e,circ}$ of 1.9 ± 0.2 kpc, and the typical upper limit of 39 unresolved sources is $R_{\rm e,circ}<1.5$ kpc. Therefore, we conclude that the typical size of (less obscured) stellar continua of H-faint galaxies should be less than 1.5 kpc, slightly lower than the $R_{\rm e}=2$ kpc size obtained on the stacked F160W images of galaxies at $H_{160}-m_{4.5}>2.25$ in the sample of (Wang et al. 2016, note that F160W non-detection was not required for this sample). This is much smaller than the F160W size of ALESS SMGs at $z=1\sim3$ ($R_{\rm e,circ}\sim3.1$ kpc assuming median $b/a=0.5$; Chen et al. 2015) in which no dependence on redshift was identified, suggesting no significant extended stellar disk component ($R_{\rm e}\gtrsim3$ kpc) in the majority of H-faint galaxies unlike those in near-IR-bright SMGs.

We note that although IRAC/CH2 samples the rest-frame z-band stellar continuum emissions for H-faint galaxies at $z\sim4$, it is still possible that a more compact and obscured stellar component could remain undetected at the dust continuum centroid (e.g., Simpson et al. 2017b; Lang et al. 2019; Sun et al. 2021). Therefore, the true stellar-mass profile can be more compact than the 4.5 μm light profile. The likely existence of such a fully dust-obscured stellar component is also consistent with previous findings that the A_V of SMGs can be underestimated through energy-balance SED modeling (e.g., Casey et al. 2014b).

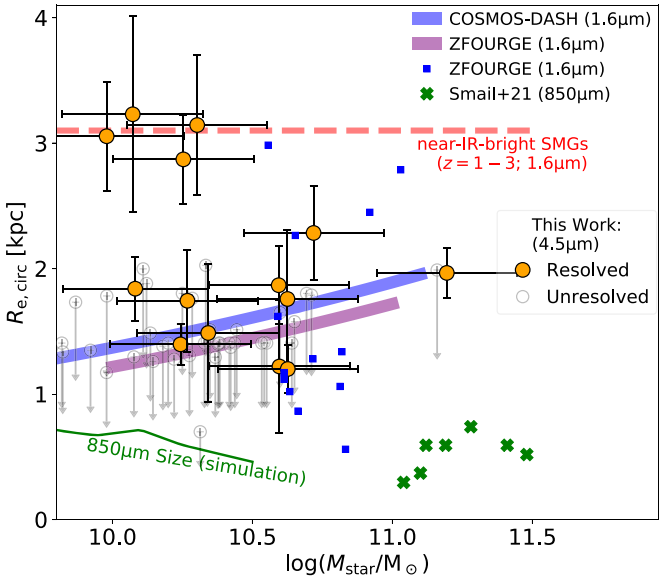

Figure 7. Circularized effective radii vs. stellar masses. The orange-filled circles denote resolved H-faint galaxies in this work, and the transparent open circles represent the upper limits for unresolved sources, assuming $R_{\rm e,circ}<0\farcs3\,\mu^{-0.5}$. The reference samples that we plot include (i) star-forming ZFOURGE galaxies at $z\sim3.8$ (the blue squares: Straatman et al. 2015; the purple line: Allen et al. 2017; 1.6 μm sizes), (ii) star-forming galaxies at $z=4$ inferred from COSMOS-DASH (the blue line: Mowla et al. 2019, scaled from $z=2.75$), and (iii) near-IR-bright ALESS SMGs at $z\simeq1$–3 (the red dashed line: Chen et al. 2015, 1.6 μm sizes). We also compare the 850 μm dust continuum sizes and stellar masses of K-faint SMGs (the green crosses; observed by Smail et al. 2021) and star-forming galaxies (the green solid line; simulated by Popping et al. 2021) at similar redshift.

Gullberg et al. (2019) measured a median dust continuum size of $R_{\rm e,circ} = 0.6 \pm 0.1$ kpc for seven K-faint SMGs at 870 μm (Smail et al. 2021; note that extended halos/disks might not be bright enough to be detected individually with these works). This is found to be more compact than those of near-IR-bright SMGs at similar redshifts with comparable $M_{\rm star}$ and $M_{\rm dust}$ but lower A_V. As also suggested in Smail et al. (2021), we argue that the compactness of both dust and stellar continua ($R_{\rm e} \sim 1$ kpc) are likely the cause of high dust attenuation inferred from the SEDs of H-faint galaxies. With no significant evolution in the dust continuum size versus redshift (e.g., Gullberg et al. 2019; Tadaki et al. 2020) and $\sim(1+z)^{-1}$ evolution in the stellar continuum size (e.g., Mosleh et al. 2012; van der Wel et al. 2014; Mowla et al. 2019), SMGs at a higher redshift ($z \sim 4$) are more likely to host compact dust and stellar continua of similar size than those at lower redshifts ($z = 1 \sim 2$ where the difference in $R_{\rm e,star}$ and $R_{\rm e,dust}$ can be around 2 kpc; e.g., Hodge et al. 2016; Lang et al. 2019; Franco et al. 2020; Sun et al. 2021), producing highly obscured stellar continua in the optical/near-IR bands. Most recently, Popping et al. (2021) also reported a comparable size of stellar and dust continua for star-forming galaxies at $z \sim 4$ using TNG50 simulation. Further ALMA continuum observations on these cluster-lensed H-faint galaxies will test this interpretation directly.

We do not observe any clear correlation between the effective radii and stellar masses of resolved H-faint sources. The four sources at $R_{\rm e,circ} > 2.5$ kpc are less massive (mean $M_{\rm star} = 10^{10.2\pm0.1}\ M_\odot$) than the compact but resolved sample ($10^{10.5\pm0.2}\ M_\odot$). Sources with relatively large $R_{\rm e,circ}$ may represent galaxies in the final coalescence phase of merger (e.g., see the saddle-like shape in the contours of ES-016; Figure 1). Such an interpretation can be tested with future high-resolution ALMA or JWST observations.

We compared the $R_{\rm e,circ} - M_{\rm star}$ distribution with massive star-forming galaxies ($>10^{10}\ M_\odot$) at $z \sim 4$ reported in the literature, including the ZFOURGE sample (Straatman et al. 2015; Allen et al. 2017) and the COSMOS-DASH sample (Mowla et al. 2019; note that we extrapolate the best-fit relation at $z = 2.75$ to $z = 4$ by a scale factor of $(1+z)^{-1}$ and assume a typical axis ratio of $b/a = 0.5$). We find that the effective radii of H-faint galaxies are in good agreement with those of H-selected star-forming galaxies. This suggests that H-faint galaxies represent the massive and dusty tail of the distribution of the wider galaxy population at $z \sim 4$ instead of a distinct class.

4.5. Number Density of H-faint Sources

Figure 8 shows the cumulative number count of H-faint galaxies presented in this work (lensed sample) and Wang et al. (2019, unlensed sample) as a function of IRAC CH2 magnitude. Compared with this blind survey in the CANDELS fields (the effective survey area is $\sim$300 arcmin^2), we have discovered $\sim$10 times more bright H-faint galaxies at CH2$<$22 owing to the lensing magnification. After correcting for magnification of each source, the two number count functions are similar, especially in the range of $22 <$ CH2 < 23.5. At the faint end (CH2 > 23.5), the source count derived in our sample is lower. This is because the detection of intrinsically faint sources requires a larger lensing magnification for a smaller survey area (see the lower-right panel of Figure 10 in Appendix A).

We then estimate the surface number density of H-faint galaxies. The apparent total survey area of the 101 cluster fields in the F160W band is summed to be 648 arcmin^2. With the

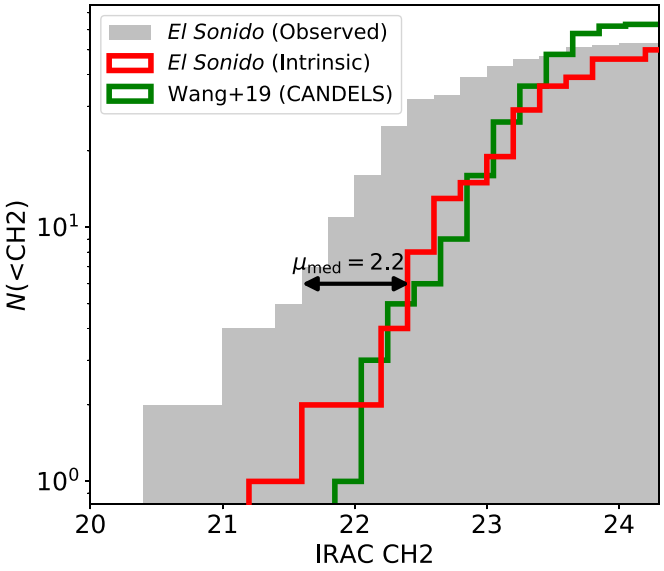

Figure 8. Cumulative number counts of H-faint sources presented in this work and (Wang et al. 2019, green solid line) as a function of IRAC CH2 magnitude. The gray-filled histogram denotes the cumulative distribution of directly observed CH2 magnitude (i.e., without lensing correction), and the red solid line denotes the distribution of magnification-corrected CH2 magnitude. Although we discover $\sim$10 times more bright H-faint sources at CH2 $>$22 than Wang et al. (2019), the source count as a function of lensing-corrected CH2 brightness is consistent with that derived in the CANDELS fields.

estimated completeness ratio ($C \sim 76\%$) and the cumulative effective survey area as a function of intrinsic CH2 magnitude threshold (i.e., $A_{\rm eff}$(CH2); on the source plane) as detailed in Appendix B, we derive a maximum intrinsic survey area of $\sim$221 arcmin^2. This can be further reduced to $\sim$120 arcmin^2 at CH2 $= 24$ because a larger magnification is required to detect fainter sources, limiting the effective survey area. Based on the differential number count and effective survey area, both as functions of intrinsic CH2 magnitude, we derive a surface number density of H-faint sources (intrinsic CH2 $\leqslant 24$ and $H_{160} \gtrsim 27.2$) of $(7.9 \pm 2.2) \times 10^2$ deg^{-2}. Note that each multiply imaged system has been treated as one source in this calculation.

Assuming an ALMA detection rate ($S_{870} > 0.6$ mJy) of $62\% \pm 6\%$ as reported in Wang et al. (2019), we would expect a surface density of ALMA-bright H-faint galaxies as $(4.9 \pm 1.4) \times 10^2$ deg^{-2}. This is consistent with the measured density of ALMA-detected H-faint galaxies ($\sim$530 deg^{-2}, Wang et al. 2019) and $K > 25.3$, $S_{870} \geqslant 1$ mJy SMGs (450^{+750}_{-300} deg^{-2}, Smail et al. 2021).

4.6. Contribution to the CSFRD and SMF

If $80\% \pm 9\%$ of the H-faint galaxies (i.e., the fraction of MIPS-faint sources) are in the redshift range of $z \simeq 3-5$, we can then estimate their contribution to the cosmic SFR density (CSFRD) as $\psi = 10^{-2.5\pm0.3}\ M_\odot\ {\rm yr}^{-1}\ {\rm Mpc}^{-3}$, corresponding to $8^{+8}_{-4}\%$ of the CSFRD at this epoch (Madau & Dickinson 2014). Survey completeness has been corrected for this CSFRD calculation. As shown in the left panel of Figure 9, such a contribution is consistent with that of H-faint galaxies reported previously (Yamaguchi et al. 2019; Wang et al. 2019), and also comparable to that of AS2UDS SMGs at $z \sim 4$ ($S_{870} > 1$ mJy, i.e., $L_{\rm IR} > 10^{12}\ L_\odot$) reported in Dudzevičiūtė et al. (2020).

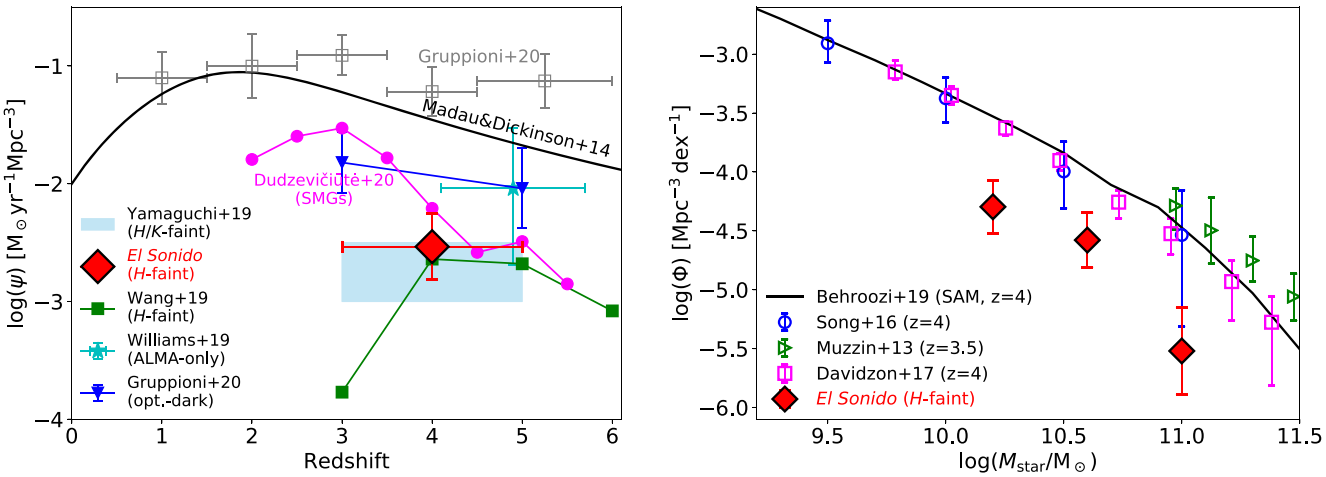

Figure 9. Left: CSFRD contribution of *H*-faint galaxies presented in this work (red diamonds). CSFRD contribution of *H*-faint galaxies found by Yamaguchi et al. (2019) and Wang et al. (2019), optical/near-IR-dark galaxies found by Williams et al. (2019) and Gruppioni et al. (2020), as well as AS2UDS SMGs ($S_{870} > 1$ mJy; Dudzevičiūtė et al. 2020) are also shown for comparison. The ALMA-based CSFRD evolution measured by Gruppioni et al. (2020) is shown as gray open squares. The analytic model by Madau & Dickinson (2014) is shown as a black solid line. Right: The contribution of *H*-faint galaxies to the galaxy SMF at $z \sim 4$. Unobscured galaxies selected by HST (Song et al. 2016; the blue open circles), VISTA/K_S (Muzzin et al. 2013; the green open triangles), and K + CH1 (Davidzon et al. 2017; the magenta open squares) are shown for comparison. Black solid line denotes the SMF derived with a semi-analytic model (Behroozi et al. 2019).

We further notice that the contribution to the CSFRD from *H*-faint galaxies in this work is about three times lower than the values suggested by Williams et al. (2019) and Gruppioni et al. (2020) through serendipitous ALMA detections in relatively smaller survey areas (one source in 8 arcmin^2 and seven sources in 25 arcmin^2, respectively). An average near-IR magnitude of 23.7 ± 0.1 can be measured from the stacked UltraVISTA $YJHK_S$ data for the sample of Gruppioni et al. (2020), suggesting the potential detectability of these sources with deeper F160W data (e.g., at a depth comparable to those of this work (also Yamaguchi et al. 2019; Wang et al. 2019)), and thus the estimate of CSFRD may be consistent. Furthermore, as argued by Zavala et al. (2021), possible clustering of serendipitous sources around main ALPINE targets can also be a concern in Gruppioni et al. (2020) sample.

We also evaluate the contribution to the SMF at $z \sim 4$ from the *H*-faint galaxies in the right panel of Figure 9. In the three stellar-mass bins from 10^{10} to $10^{11.2}$ $M_\odot$, *H*-faint galaxies contribute to 16^{+13}_{-7}% of the volume densities ($10^{-4.3\pm0.2}$, $10^{-4.6\pm0.2}$, and $10^{-5.5\pm0.4}$ Mpc^{-3} dex^{-1}) that are derived based on unobscured near-IR-selected galaxies at comparable redshift (Muzzin et al. 2013; Song et al. 2016; Davidzon et al. 2017), consistent with the fraction reported by Alcalde Pampliega et al. (2019). We note that Caputi et al. (2015) and Alcalde Pampliega et al. (2019) suggested a higher contribution of K/*H*-faint IRAC sources to the most massive ($M_{\rm star} > 10^{11}$ $M_\odot$) galaxy population at $z > 4$. Although only two sources in our sample (ES-009 and ES-050) are found in this parameter space because of the limited survey area, different selection criteria and assumption of SFH, we may tentatively estimate a fraction of *H*-faint galaxies at $M_{\rm star} > 10^{11}$ $M_\odot$ as 15^{+21}_{-8}%, consistent with the value reported by (Alcalde Pampliega et al. 2019, $27\% \pm 17\%$ at $4 < z < 5$).

5. Summary

We have conducted a Spitzer/IRAC survey of *H*-faint ($H_{160} \gtrsim 26.4$, $< 5\sigma$) galaxies in 101 lensing cluster fields over a total survey area of 648 arcmin^2 (effectively ~221 arcmin^2 on the source plane), including all of the 68 best studied massive galaxy clusters observed with the HST Large/Treasury Programs: HFF (BUFFALO), CLASH, and RELICS. Using imaging data obtained with HST/WFC3-IR, Spitzer/IRAC and MIPS, Herschel/PACS and SPIRE, we have carried out photometric measurements, surface brightness profile modeling, stacking analysis, and near-to-far-IR (1.05–500 μm) SED modeling of the selected *H*-faint galaxies. The main results of this study are the following:

1. We have detected 53 (48 independent) *H*-faint galaxies in 32 cluster fields. With a median IRAC/CH2 magnitude of 22.46 ± 0.11, all of these sources show a red near-IR color of $H_{160} - {\rm CH2} > 2.5$ (the median is above 3.9) assuming a point-source spatial profile. The median IRAC CH1–CH2 color is 0.49 ± 0.03, suggesting a reddened stellar continuum.
2. We were able to resolve 14 out of the 53 sources in the IRAC CH2 band thanks to the gravitational lensing. The mean circularized effective radius of the resolved sources is $0\farcs46 \pm 0\farcs04$, corresponding to a physical scale of 1.9 ± 0.2 kpc at $z = 4$ after lensing magnification correction. Considering the unresolved sources, the median stellar continuum size of *H*-faint galaxies is very compact ($R_{\rm e,circ} < 1.5$ kpc).
3. We estimate the photometric redshift of *H*-faint galaxies with the stacked near-IR SEDs. The majority ($80\% \pm 9\%$) of *H*-faint galaxies are faint in the MIPS 24 μm band (<17 μJy), and the derived $z_{\rm phot} = 3.6^{+0.4}_{-0.3}$ is consistent with those of optical/near-IR-dark galaxies reported previously. A small fraction of sources in this study ($20\% \pm 9\%$) are bright at 24 μm (127 ± 12 μJy), and they are likely located at a lower redshift ($z_{\rm phot} = 2.6 \pm 0.4$).
4. After correcting for the lensing magnification, we show that the *H*-faint galaxies in this study are massive (median $M_{\rm star} = 10^{10.3\pm0.3}$ $M_\odot$), strongly star-forming (SFR $= 100^{+60}_{-40}$ $M_\odot$ yr^{-1}), and highly dust-obscured ($A_V = 2.6 \pm 0.3$). The assumption of star formation history (i.e., with or without a late starburst) is critical for the characterization of SFR and

stellar mass, which can result in a factor of about seven times difference.

5. The most remarkable source in our sample, ES-009 in the field of A2813, is the brightest *H*-faint galaxy at 4.5 μm known so far (CH2 $= 20.48 \pm 0.03$). This galaxy is detected in all eight available bands at $\lambda \geqslant 3.6$ μm up to 500 μm, and likely hosts a stellar mass of $10^{11.2\pm0.2}$ $M_{\odot}$, SFR of 500^{+290}_{-180} $M_{\odot}$ yr^{-1} at $z_{\rm phot} = 3.2 \pm 0.1$.
6. We conclude that the highly obscured stellar continuum of *H*-faint galaxies at $z \sim 4$ is likely caused by the compactness of both the stellar and dust components ($R_{\rm e,circ} \sim 1$ kpc; see Smail et al. 2021). The stellar continuum sizes of *H*-faint galaxies are in general agreement with those of massive unobscured galaxies at similar redshifts, suggesting that *H*-faint galaxies represent the massive and dusty tail of the distribution of the wider galaxy population at $z \sim 4$.
7. We derive a sky surface density of $(7.9 \pm 2.2) \times 10^2$ deg^{-2} for Wang et al. (2019)-like *H*-faint galaxies in lensing cluster fields. This number is consistent with the reported density of *H*-faint galaxies measured in blank fields (CANDELS, Wang et al. 2019) and *K*-faint SMGs (Smail et al. 2021) if ~40% of *H*-faint galaxies are less active and faint at 870 μm ($S_{870} < 0.6$ mJy). We further conclude that *H*-faint galaxies contribute to 8^{+8}_{-4}% of the cosmic SFR density at $z = 3 \sim 5$, and account for 16^{+13}_{-7}% of the galaxies in the stellar-mass range of $10^{10} - 10^{11.2}$ $M_{\odot}$ at this epoch.

This extensive lensing survey of optical and near-infrared dark objects (El Sonido) yields a bright sample of *H*-faint galaxies, owing to cluster lensing magnification, with rich ancillary data from the optical to far-IR wavelengths. Future observations with ALMA and JWST will provide key insights of the dust and (less obscured) stellar continua of these dusty and massive galaxies at $z \sim 4$, which are typically missed in HST-based surveys or certain "stellar-mass"-selected galaxy samples, improving our understanding of their physical properties (i.e., dust mass, dust temperature, dust/stellar continuum size) and formation history.

We thank the anonymous referee for helpful comments. F.S. and E.E. acknowledge funding from JWST/NIRCam contract to the University of Arizona, NAS5-02105. P.G.P.G. acknowledges support from Spanish Government grant PGC2018-093499-B-I00. I.R.S. acknowledges support from STFC (ST/T000244/1). K.I.C. acknowledges funding from the European Research Council through the award of the Consolidator Grant ID 681627-BUILDUP. G.E.M. acknowledges the Villum Fonden research grant 37440, "The Hidden Cosmos" and the Cosmic Dawn Center of Excellence funded by the Danish National Research Foundation under then grant No. 140. M.J. is supported by the United Kingdom Research and Innovation (UKRI) Future Leaders Fellowship "Using Cosmic Beasts to uncover the Nature of Dark Matter" (grant number MR/S017216/1).

This work is based on observations made with the Spitzer Space Telescope, which was operated by the Jet Propulsion Laboratory, California Institute of Technology under a contract with NASA.

This work is based on observations made with the NASA/ESA Hubble Space Telescope, obtained from the data archive at the Space Telescope Science Institute.

This work utilizes gravitational lensing models produced by PIs Bradač Natarajan & Kneib (CATS), Merten & Zitrin, Sharon, Williams, Keeton, Bernstein, and Diego, and the GLAFIC group. This lens modeling was partially funded by the HST Frontier Fields program conducted by STScI. STScI is operated by the Association of Universities for Research in Astronomy, Inc. under NASA contract NAS 5-26555. The lens models were obtained from the Mikulski Archive for Space Telescopes (MAST).

This work is based on observations made with Herschel. Herschel is an ESA space observatory with science instruments provided by European-led Principal Investigator consortia and with important participation from NASA.

Facilities: HST(WFC3), Spitzer(IRAC and MIPS), Herschel (PACS and SPIRE).

Software: astropy (Astropy Collaboration et al. 2013), CIGALE (Noll et al. 2009; Boquien et al. 2019), EAZY (Brammer et al. 2008), GALFIT (Peng et al. 2010), MAGPHYS (da Cunha et al. 2008; Battisti et al. 2019), Photutils (Bradley et al. 2020), SExtractor (Bertin & Arnouts 1996).

Appendix A
Depths of the 101 Lensing Cluster Fields

In each lensing cluster field, the 5σ depths of the WFC3-IR/F160W and IRAC/CH2 data in their overlapped area are measured using randomly distributed apertures. The aperture sizes and aperture-correction factors are identical to those that we adopted to obtain photometric measurements of *H*-faint sources. Table 1 summarizes the depths of data in all 101 cluster fields. The 16th, 50th, and 84th percentiles of the 5σ depths are 26.2, 26.4, and 26.7 in the F160W band and 22.8, 23.1, and 23.5 in the CH2 band. The left panel of Figure 10 shows the distribution of depths in these two bands. Excluding the six HFF/BUFFALO clusters, where the apparent survey area per cluster field is about four times the typical ones (i.e., with only one WFC3-IR pointing), we find no clear difference in the data depth among the cluster fields with and without *H*-faint galaxies through a Kolmogorov–Smirnov (K-S) test.

We also evaluate the influence of F160W or CH2 source densities on *H*-faint galaxy selection. We have run SExtractor in these fields and found a median surface density of $\Sigma_{1.6} = 0.057$ arcsec^{-2} and $\Sigma_{4.5} = 0.014$ arcsec^{-2} for F160W and CH2 sources at S/N > 5, respectively. A K-S test suggests no difference in source densities among cluster fields with and without *H*-faint galaxies. The cumulative number of *H*-faint galaxies versus the angular distance to the cluster center can be well characterized with a simple quadratic function ($N \propto r^2$) at $r < 1\farcm4$, i.e., within the FoV of one WFC3-IR pointing. This further suggests that the increasing source density toward the cluster center does not have a significant influence on the *H*-faint source selection.

Appendix B
Completeness and Intrinsic Survey Area

We first estimate the completeness of our *H*-faint galaxy selection. Because we only surveyed *H*-faint sources that are >1″ away from HST sources and distinguishable from other IRAC sources (i.e., >1.″8 away according to the Rayleigh criterion), we correct the survey area in each field by a factor of $\exp[-(\Sigma_{1.6} - \Sigma_{4.5})\pi r_{1.6}^2 - \Sigma_{4.5}\pi r_{4.5}^2]$ where $r_{1.6} = 1''$ and $r_{4.5} = 1\farcs8$. Based on the elliptical parameters of sources derived with SExtractor, we find that bright and extended ($R_{\rm e,maj} \gtrsim 1''$) galaxies in the fields can only lead to a minor

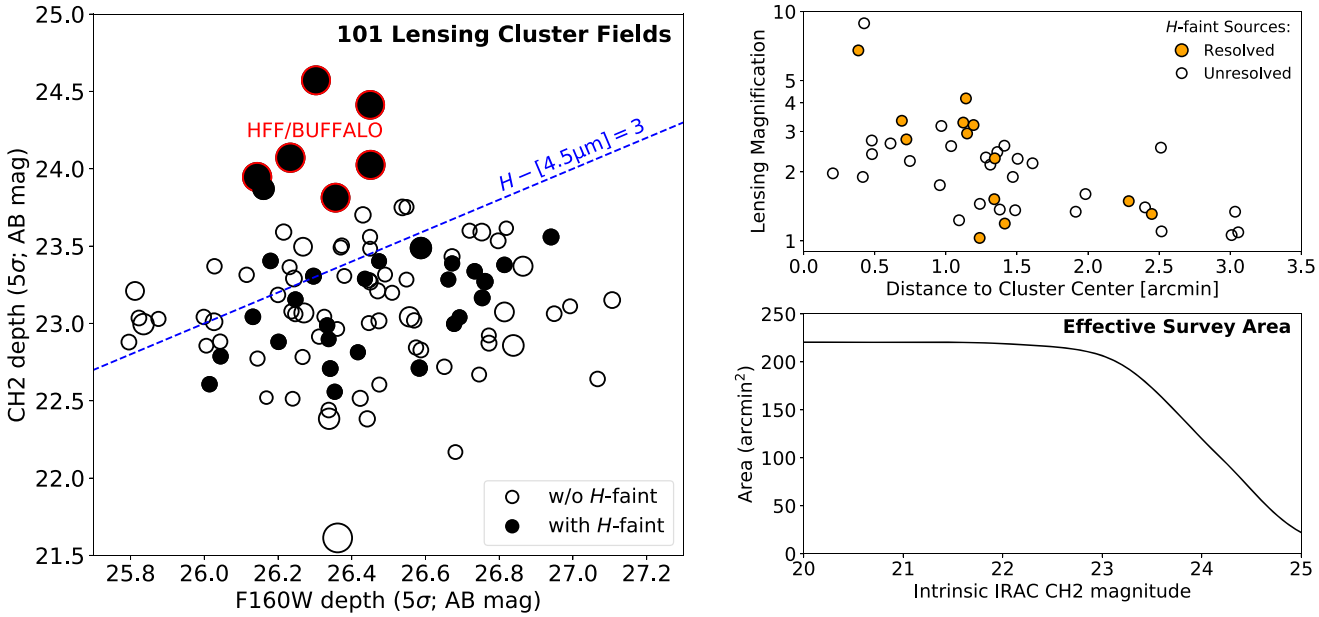

Figure 10. Left: depths of imaging data in the IRAC/CH2 and WFC3-IR/F160W band. The 32 cluster fields in which we detected *H*-faint galaxies are shown as black filled circles, and the remaining 69 fields are shown as empty ones. Larger circle sizes indicate larger apparent survey areas. Six HFF/BUFFALO clusters are marked as circles with red edges. *H*-faint galaxies discovered in clusters below the blue dashed line are automatically at $H_{160} - \mathrm{CH2} > 3$. Top right: lensing magnifications of *H*-faint galaxies vs. their distances to the corresponding cluster centers. Orange-filled circles denote resolved sources and open circles denote unresolved sources. Bottom right: cumulative effective survey area in the source plane as a function of intrinsic IRAC/CH2 magnitude threshold. The effective survey area is 120 arcmin^2 for sources at an intrinsic depth of CH2 = 24.

reduction of the effective survey area by ∼1%. We then derive an effective survey area of 490 arcmin^2 in the image plane. This implies that ∼24% of the *H*-faint galaxies will be missed in our survey due to the existence of nearby field sources, for example, the triply imaged *H*-faint ALMA-bright galaxy at $z = 4.3$ behind the cluster 0102–4915 (Caputi et al. 2021).

We also note that *H*-faint sources are often found with less obscured companions detectable with HST (e.g., Simpson et al. 2017a; Schreiber et al. 2018b; Caputi et al. 2021). Adopting the angular cross-correlation function between *H*-faint and rest-frame-UV-selected galaxies at similar photometric redshifts reported in Wang et al. (2019) and the surface density of $H < 27.3$ galaxies at $z \simeq 3$–5 within the GOODS field (Barro et al. 2019), the surface density of UV-bright companion galaxies within 1″ from *H*-faint sources is around 0.004 arcsec^{-2}, i.e., one order of magnitude lower than random field sources. Therefore, the additional clustering effect of *H*-faint and companion galaxies will not be a concern for our completeness calculation.

Based on the lens models described in Section 4.2, we derive the cumulative effective survey area in the source plane as a function of magnification threshold (i.e., $A_{\mathrm{eff}}(\mu)$) in each cluster field. For cluster fields without available lens models, we used the median of $A_{\mathrm{eff}}(\mu)$ curves for approximation (scaled to the survey area of these fields). These functions are further converted to A_{eff}(CH2), i.e., functions of intrinsic CH2 magnitude threshold, according to the CH2 depths of corresponding cluster fields. The cumulative effective survey area, after lensing correction, as a function of intrinsic CH2 magnitude threshold in the 101 cluster fields is shown in the lower-right panel of Figure 10. With a maximum at ∼221 arcmin^2, the intrinsic survey area is reduced to ∼120 arcmin^2 at an intrinsic depth of CH2 = 24.

Based on the synthesized $A_{\mathrm{eff}}(\mu)$ curve and the 53-source sample size, we anticipate to detect 3.4 sources in the area with a lensing magnification of $\mu > 5$, and 0.5 source with $\mu > 10$. Both expectations are consistent with the observed numbers of strongly lensed *H*-faint galaxies (two at $\mu > 10$ and zero at $\mu > 10$). Therefore, we further conclude that the selection bias against strongly lensed (and therefore extended) sources should be negligible.

ORCID iDs

Fengwu Sun https://orcid.org/0000-0002-4622-6617
Pablo G. Pérez-González https://orcid.org/0000-0003-4528-5639
Ian Smail https://orcid.org/0000-0003-3037-257X
Karina I. Caputi https://orcid.org/0000-0001-8183-1460
Franz E. Bauer https://orcid.org/0000-0002-8686-8737
Timothy D. Rawle https://orcid.org/0000-0002-7028-5588
Seiji Fujimoto https://orcid.org/0000-0001-7201-5066
Kotaro Kohno https://orcid.org/0000-0002-4052-2394
Matteo Bianconi https://orcid.org/0000-0002-0427-5373
Francoise Combes https://orcid.org/0000-0003-2658-7893
Mathilde Jauzac https://orcid.org/0000-0003-1974-8732
Anton M. Koekemoer https://orcid.org/0000-0002-6610-2048
Georgios E. Magdis https://orcid.org/0000-0002-4872-2294
Giulia Rodighiero https://orcid.org/0000-0002-9415-2296
Wiphu Rujopakarn https://orcid.org/0000-0002-0303-499X
Daniel Schaerer https://orcid.org/0000-0001-7144-7182
Charles L. Steinhardt https://orcid.org/0000-0003-3780-6801
Paul Van der Werf https://orcid.org/0000-0001-5434-5942
Gregory L. Walth https://orcid.org/0000-0002-6313-6808
John R. Weaver https://orcid.org/0000-0003-1614-196X

References

Alcalde Pampliega, B., Pérez-González, P. G., Barro, G., et al. 2019, ApJ, 876, 135
Allen, R. J., Kacprzak, G. G., Glazebrook, K., et al. 2017, ApJL, 834, L11

Astropy Collaboration, Robitaille, T. P., Tollerud, E., et al. 2013, A&A, 558, A33
Bakx, T. J. L. C., Tamura, Y., Hashimoto, T., et al. 2020, MNRAS, 493, 4294
Barro, G., Pérez-González, P. G., Cava, A., et al. 2019, ApJS, 243, 22
Battisti, A. J., da Cunha, E., Grasha, K., et al. 2019, ApJ, 882, 61
Behroozi, P., Wechsler, R. H., Hearin, A. P., & Conroy, C. 2019, MNRAS, 488, 3143
Bertin, E., & Arnouts, S. 1996, A&AS, 117, 393
Bertoldi, F., Carilli, C. L., Menten, K. M., et al. 2000, A&A, 360, 92
Boquien, M., Burgarella, D., Roehlly, Y., et al. 2019, A&A, 622, A103
Bouwens, R., González-López, J., Aravena, M., et al. 2020, ApJ, 902, 112
Bradley, L., Sipőcz, B., Robitaille, T., et al. 2020, astropy/photutils: v1.0.0, Zenodo, doi:10.5281/zenodo.4044744
Brammer, G. B., van Dokkum, P. G., & Coppi, P. 2008, ApJ, 686, 1503
Calzetti, D., Armus, L., Bohlin, R. C., et al. 2000, ApJ, 533, 682
Caputi, K. I., Caminha, G. B., Fujimoto, S., et al. 2021, ApJ, 908, 146
Caputi, K. I., Dunlop, J. S., McLure, R. J., et al. 2012, ApJL, 750, L20
Caputi, K. I., Ilbert, O., Laigle, C., et al. 2015, ApJ, 810, 73
Caputi, K. I., Michałowski, M. J., Krips, M., et al. 2014, ApJ, 788, 126
Casey, C. M., Narayanan, D., & Cooray, A. 2014a, PhR, 541, 45
Casey, C. M., Scoville, N. Z., Sanders, D. B., et al. 2014b, ApJ, 796, 95
Chabrier, G. 2003, PASP, 115, 763
Chapman, S. C., Lewis, G. F., Scott, D., Borys, C., & Richards, E. 2002, ApJ, 570, 557
Chapman, S. C., Richards, E. A., Lewis, G. F., Wilson, G., & Barger, A. J. 2001, ApJL, 548, L147
Charlot, S., & Fall, S. M. 2000, ApJ, 539, 718
Chen, C.-C., Smail, I., Swinbank, A. M., et al. 2015, ApJ, 799, 194
Coe, D., Salmon, B., Bradač, M., et al. 2019, ApJ, 884, 85
Cowie, L. L., Barger, A. J., Wang, W. H., & Williams, J. P. 2009, ApJL, 697, L122
da Cunha, E., Charlot, S., & Elbaz, D. 2008, MNRAS, 388, 1595
da Cunha, E., Walter, F., Smail, I. R., et al. 2015, ApJ, 806, 110
Dannerbauer, H., Lehnert, M. D., Lutz, D., et al. 2002, ApJ, 573, 473
Davidzon, I., Ilbert, O., Laigle, C., et al. 2017, A&A, 605, A70
Dey, A., Graham, J. R., Ivison, R. J., et al. 1999, ApJ, 519, 610
Dudzevičiūtė, U., Smail, I., Swinbank, A. M., et al. 2020, MNRAS, 494, 3828
Dudzevičiūtė, U., Smail, I., Swinbank, A. M., et al. 2021, MNRAS, 500, 942
Dunlop, J. S., McLure, R. J., Yamada, T., et al. 2004, MNRAS, 350, 769
Egami, E., Rex, M., Rawle, T. D., et al. 2010, A&A, 518, L12
Fazio, G. G., Hora, J. L., Allen, L. E., et al. 2004, ApJS, 154, 10
Franco, M., Elbaz, D., Béthermin, M., et al. 2018, A&A, 620, A152
Franco, M., Elbaz, D., Zhou, L., et al. 2020, A&A, 643, A53
Frayer, D. T., Reddy, N. A., Armus, L., et al. 2004, AJ, 127, 728
Frayer, D. T., Smail, I., Ivison, R. J., & Scoville, N. Z. 2000, AJ, 120, 1668
Fujimoto, S., Ouchi, M., Kohno, K., et al. 2018, ApJ, 861, 7
Fujimoto, S., Ouchi, M., Ono, Y., et al. 2016, ApJS, 222, 1
Gaia Collaboration, Brown, A. G. A., Vallenari, A., et al. 2018, A&A, 616, A1
Gonzaga, S., Hack, W., Fruchter, A., & Mack, J. 2012, The DrizzlePac Handbook (Baltimore, MD: STScI)
Griffin, M. J., Abergel, A., Abreu, A., et al. 2010, A&A, 518, L3
Grogin, N. A., Kocevski, D. D., Faber, S. M., et al. 2011, ApJS, 197, 35
Gruppioni, C., Béthermin, M., Loiacono, F., et al. 2020, A&A, 643, A8
Gullberg, B., Smail, I., Swinbank, A. M., et al. 2019, MNRAS, 490, 4956
Hodge, J. A., & da Cunha, E. 2020, RSOS, 7, 200556
Hodge, J. A., Swinbank, A. M., Simpson, J. M., et al. 2016, ApJ, 833, 103
Huang, J. S., Zheng, X. Z., Rigopoulou, D., et al. 2011, ApJL, 742, L13
Hughes, D. H., Serjeant, S., Dunlop, J., et al. 1998, Natur, 394, 241
Hurley, P. D., Oliver, S., Betancourt, M., et al. 2017, MNRAS, 464, 885
Ivison, R. J., Greve, T. R., Serjeant, S., et al. 2004, ApJS, 154, 124
Iyer, K. G., Tacchella, S., Genel, S., et al. 2020, MNRAS, 498, 430
Jauzac, M., Clément, B., Limousin, M., et al. 2014, MNRAS, 443, 1549
Jauzac, M., Richard, J., Jullo, E., et al. 2015, MNRAS, 452, 1437
Jauzac, M., Richard, J., Limousin, M., et al. 2016, MNRAS, 457, 2029
Kawamata, R., Oguri, M., Ishigaki, M., Shimasaku, K., & Ouchi, M. 2016, ApJ, 819, 114
Kennicutt, R. C. J. 1998, ARA&A, 36, 189
Kirkpatrick, A., Pope, A., Sajina, A., et al. 2015, ApJ, 814, 9
Kirkpatrick, J. D., Gelino, C. R., Faherty, J. K., et al. 2021, ApJS, 253, 7
Koekemoer, A. M., Faber, S. M., Ferguson, H. C., et al. 2011, ApJS, 197, 36
Lagattuta, D. J., Richard, J., Bauer, F. E., et al. 2019, MNRAS, 485, 3738
Lang, P., Schinnerer, E., Smail, I., et al. 2019, ApJ, 879, 54
Leja, J., Carnall, A. C., Johnson, B. D., Conroy, C., & Speagle, J. S. 2019, ApJ, 876, 3
Limousin, M., Richard, J., Jullo, E., et al. 2016, A&A, 588, A99
Lotz, J. M., Koekemoer, A., Coe, D., et al. 2017, ApJ, 837, 97
Lutz, D., Poglitsch, A., Altieri, B., et al. 2011, A&A, 532, A90
Madau, P., & Dickinson, M. 2014, ARA&A, 52, 415
Mahler, G., Richard, J., Clément, B., et al. 2018, MNRAS, 473, 663
Marrone, D. P., Spilker, J. S., Hayward, C. C., et al. 2018, Natur, 553, 51
McCarthy, P. J. 2004, ARA&A, 42, 477
Merten, J., Coe, D., Dupke, R., et al. 2011, MNRAS, 417, 333
Mitsuhashi, I., Matsuda, Y., Smail, I., et al. 2021, ApJ, 907, 122
Mosleh, M., Williams, R. J., Franx, M., et al. 2012, ApJL, 756, L12
Mowla, L. A., van Dokkum, P., Brammer, G. B., et al. 2019, ApJ, 880, 57
Muzzin, A., Marchesini, D., Stefanon, M., et al. 2013, ApJ, 777, 18
Noll, S., Burgarella, D., Giovannoli, E., et al. 2009, A&A, 507, 1793
Oguri, M. 2010, PASJ, 62, 1017
Okabe, T., Oguri, M., Peirani, S., et al. 2020, MNRAS, 496, 2591
Oke, J. B., & Gunn, J. E. 1983, ApJ, 266, 713
Oliver, S. J., Bock, J., Altieri, B., et al. 2012, MNRAS, 424, 1614
Peng, C. Y., Ho, L. C., Impey, C. D., & Rix, H.-W. 2010, AJ, 139, 2097
Poglitsch, A., Waelkens, C., Geis, N., et al. 2010, A&A, 518, L2
Popping, G., Pillepich, A., Calistro Rivera, G., et al. 2021, arXiv:2101.12218
Postman, M., Coe, D., Benítez, N., et al. 2012, ApJS, 199, 25
Rawle, T. D., Altieri, B., Egami, E., et al. 2016, MNRAS, 459, 1626
Richard, J., Jauzac, M., Limousin, M., et al. 2014, MNRAS, 444, 268
Riechers, D. A., Bradford, C. M., Clements, D. L., et al. 2013, Natur, 496, 329
Rieke, G. H., Young, E. T., Engelbracht, C. W., et al. 2004, ApJS, 154, 25
Rodighiero, G., Cimatti, A., Franceschini, A., et al. 2007, A&A, 470, 21
Salim, S., & Narayanan, D. 2020, ARA&A, 58, 529
Schreiber, C., Elbaz, D., Pannella, M., et al. 2018a, A&A, 609, A30
Schreiber, C., Glazebrook, K., Nanayakkara, T., et al. 2018b, A&A, 618, A85
Schreiber, C., Pannella, M., Elbaz, D., et al. 2015, A&A, 575, A74
Simpson, J. M., Smail, I., Swinbank, A. M., et al. 2017b, ApJ, 839, 58
Simpson, J. M., Smail, I., Wang, W.-H., et al. 2017a, ApJL, 844, L10
Simpson, J. M., Swinbank, A. M., Smail, I., et al. 2014, ApJ, 788, 125
Smail, I., Dudzevičiūtė, U., Stach, S. M., et al. 2021, MNRAS, 502, 3426
Smail, I., Ivison, R. J., Kneib, J. P., et al. 1999, MNRAS, 308, 1061
Smail, I., Owen, F. N., Morrison, G. E., et al. 2002, ApJ, 581, 844
Smith, G. P., Haines, C. P., Pereira, M. J., et al. 2010, A&A, 518, L18
Song, M., Finkelstein, S. L., Ashby, M. L. N., et al. 2016, ApJ, 825, 5
Stach, S. M., Dudzevičiūtė, U., Smail, I., et al. 2019, MNRAS, 487, 4648
Steinhardt, C. L., Jauzac, M., Acebron, A., et al. 2020, ApJS, 247, 64
Stetson, P. B. 1987, PASP, 99, 191
Straatman, C. M. S., Labbé, I., Spitler, L. R., et al. 2015, ApJL, 808, L29
Straatman, C. M. S., Spitler, L. R., Quadri, R. F., et al. 2016, ApJ, 830, 51
Strandet, M. L., Weiss, A., De Breuck, C., et al. 2017, ApJL, 842, L15
Sun, F., Egami, E., Rawle, T. D., et al. 2021, ApJ, 908, 192
Tadaki, K.-i., Belli, S., Burkert, A., et al. 2020, ApJ, 901, 74
Tamura, Y., Iono, D., Wilner, D. J., et al. 2010, ApJ, 724, 1270
Tamura, Y., Mawatari, K., Hashimoto, T., et al. 2019, ApJ, 874, 27
Umehata, H., Smail, I., Swinbank, A. M., et al. 2020, A&A, 640, L8
van der Wel, A., Franx, M., van Dokkum, P. G., et al. 2014, ApJ, 788, 28
Walter, F., Decarli, R., Carilli, C., et al. 2012, Natur, 486, 233
Wang, T., Elbaz, D., Schreiber, C., et al. 2016, ApJ, 816, 84
Wang, T., Schreiber, C., Elbaz, D., et al. 2019, Natur, 572, 211
Wang, W.-H., Barger, A. J., & Cowie, L. L. 2012, ApJ, 744, 155
Wang, W.-H., Cowie, L. L., van Saders, J., Barger, A. J., & Williams, J. P. 2007, ApJL, 670, L89
Williams, C. C., Labbe, I., Spilker, J., et al. 2019, ApJ, 884, 154
Yamaguchi, Y., Kohno, K., Hatsukade, B., et al. 2019, ApJ, 878, 73
Zavala, J. A., Casey, C. M., Manning, S. M., et al. 2021, ApJ, 909, 165
Zhou, L., Elbaz, D., Franco, M., et al. 2020, A&A, 642, A155
Zitrin, A., Fabris, A., Merten, J., et al. 2015, ApJ, 801, 44
Zitrin, A., Meneghetti, M., Umetsu, K., et al. 2013, ApJL, 762, L30